EQUIVALENT CIRCUIT MODELS FOR ONE DIMENSIONAL PHOTONIC BANDGAP (PBG) STRUCTURES

by

Miodrag Kandic

A Thesis

Submitted to the Faculty of Graduate Studies

in partial fulfillment of the requirements

for the degree of

Master of Science

Department of Electrical and Computer Engineering

The University of Manitoba

THE UNIVERSITY OF MANITOBA

FACULTY OF GRADUATE STUDIES

*****

COPYRIGHT PERMISSION

EQUIVALENT CIRCUIT MODELS FOR ONE DIMENSIONAL PHOTONIC BANDGAP (PBG) STRUCTURES

BY

Miodrag Kandic

A Thesis/Practicum submitted to the Faculty of Graduate Studies of The University of Manitoba in partial fulfillment of the requirement of the degree

Of

MASTER OF SCIENCE

Acknowledgments

I would like to thank the Faculty Machinist Mr. Al Symmons for the fabrication of structures studied in this thesis. Furthermore, I would like to thank undergrad students Alex Yang and Nike Juzkiw for running the surface scan measurements in the Faculty Electromagnetic Lab. Finally I would like to acknowledge my advisor Dr. Greg Bridges for his guidance in the completion of this thesis, and the examiners Dr. Derek Oliver and Dr. Madjid Birouk for their suggestions and comments.

Abstract

This thesis explores an alternative approach for designing and analyzing one-dimensional photonic bandgap (PBG) structures and its application in microstrip transmission line filters. The one-dimensional PBG structures are spatially periodic along the axis of propagation, and they prohibit wave propagation at certain frequency ranges. In this thesis, three types of microstrip line PBG structures are studied in detail. The first PBG microstrip type studied has a substrate made of periodically contrasting dielectric layers. The equivalent circuit model for these structures is developed, consisting of cascaded transmission line sections. The second PBG microstrip type studied has circular perforations etched in the ground plane, while the dielectric substrate is homogeneous. The spacing between circles is inversely proportional to the stopband center frequency, while the circle diameters are directly proportional to the stopband bandwidth. However, the actual values for the center frequency and the bandwidth have to be determined by trial and error, using a full wave software simulation. Each microstrip structure with a homogenous substrate in this study is simulated using the Ansoft "Ensemble", commercial software based on method of moments (MoM). Several circular PBG structures are fabricated and the measured results are compared with the "Ensemble" simulation data, showing a good agreement. Furthermore, 2-D surface scans are performed on the fabricated structures, and corresponding images are studied. The final PBG microstrip type studied has rectangular ground plane perforations instead of circular ones. The rectangle width is kept constant, while the length is varied to accommodate desired bandwidth. The equivalent circuit model for these structures is

developed, consisting of cascaded transmission line sections, with the lumped element transitions in between. The equivalent circuit results are compared with the "Ensemble" simulation results of the actual structure, showing a good agreement. Therefore, the time consuming full wave simulations for rectangular ground plane PBG structures can be replaced by the proposed method.

Table of Contents

List of Figures

List of Tables

Chapter 1

Introduction

1.1 Preface

Microwave signals were traditionally transmitted through hollow metal pipes called waveguides [1], due to the absence of radiation and dielectric losses. The waveguide structures are bulky and mainly used at the frequencies in the upper microwave range, and when high-power operation is required. Whenever the frequency, or the signal power level is low enough, waveguides are replaced by printed circuits. Open printed circuit structures (microstrip, slotline, coplanar line) are generally used for the lower-frequency ranges, where the radiation is not considerable. Practically, radiation is not considerable when the structure cross sectional height is considerably smaller than the wavelength. Even though the structures under study in this thesis are based on microstrip transmission line geometry, they can be applicable to other transmission line geometries. Physically, any microstrip structure consists of a thin plate of low-loss insulating material called the substrate covered with metal completely on one side (i.e. ground plane) and partly on the other side where the circuit or antenna patterns are printed [1].

Microstrip lines are widely used in microwave applications due to their low cost, low volume, lightweight and their compatibility with integrated circuits. The radiation losses in microstrip lines become considerable at higher frequencies (cross sectional height is comparable with the wavelength) and can be reduced by choosing thinner

substrates and/or larger dielectric permittivity. Other disadvantages are in terms of low power handling capabilities, dielectric loss of guided waves and losses due to surface waves. Surface waves are trapped within dielectric substrate due to reflections at the substrate to air interface on the top and the ground plane on the bottom. On the other hand, guided waves propagate between the parallel conductors, providing the normal operation of microstrip lines. Surface waves can also produce spurious coupling between circuit or antenna elements [1]. Surface waves become significant when the substrate is thicker and has a large permittivity. Therefore, a thinner substrate will reduce both radiation and losses due to surface waves. On the other hand, the higher substrate permittivity value will increase the losses due to surface waves, but reduce the radiation loss.

Numerous applications in microstrip circuits require prohibiting wave propagation at certain frequencies and/or certain directions (as in filters or for surface wave reduction). This has created the possibility to apply the "Photonic Bandgap" Structures (i.e. PBG's) in microstrip circuits. The name for these structures comes from a specific application at visible light frequencies, where photonic crystals are used to create optical filters. Photonic crystals consist of low-loss periodic dielectric medium, where dielectric periodicity is comparable with the wavelength of filtered frequencies. However, these properties can be extended to electromagnetic waves at any frequency, by spatial scaling of the dielectric structure. Therefore, the name "Electromagnetic Bandgap" Structures (EBG's) is also used in literature. As an example, when an electromagnetic wave of proper wavelength is incident on an infinite dielectric layered structure, it can be

completely reflected. The reason is that the wave is scattered at the layer interfaces, and if the spacing is just right, the multiply-scattered waves interfere destructively inside the material [2]. If, for some frequency range, a photonic crystal reflects waves of any polarization incident at any angle, we say that the crystal has a complete photonic bandgap [2]. In order to create a material with a complete photonic bandgap, we must arrange the contrasting dielectrics in a lattice that is periodic along three axes [2]. This represents a three dimensional PBG, while 2-D and 1-D structures would have dielectric periodicity along two and one axes, respectively.

PBG's in microstrip lines don't necessarily consist of periodic contrasting dielectric substrate, most commonly holes drilled through dielectric substrate. PBG's also come in forms such as periodic patterns etched in the ground plane of microstrips, or metallic patches placed around the microstrip structure. In this thesis, the PBG structures under study are microstrip lines with etched ground plane patterns.

1.2 Thesis Objectives

The objective of this thesis is to investigate the properties of microstrip PBG structures with two different ground plane patterns, namely etched circles and etched rectangles. Both structures represent a stop band filter, which reflects signals within its stop frequency range, while passing the others. The effect of the ground plane perforations on the filter center frequency and bandwidth is investigated, for both patterns. Theoretically, in order to achieve a complete stop band within a frequency range, an infinitely long PBG structure is required. The effect of having a finite PBG structure, with different number of

periodic elements is explored and compared with the theoretical results for an infinite structure. This effect was investigated for the microstrip structure with periodic contrast in dielectric substrate, while the ground plane doesn't have any etched patterns. The main reason for investigating this type of structure is its close resemblance to the simple PBG model investigated in literature [2], consisting of an infinite multi-layered dielectric stack. This structure doesn't produce any higher order modes at the layer interfaces, unlike the etched ground pattern microstrip model, which generates those modes at the conducting discontinuities. This periodic substrate microstrip model was used for the sole purpose of investigating the effects of having a finite PBG structure, while the main scope of the thesis remains the study of microstrip line structures with etched ground plane patterns.

The microstrip line PBG structures with circular etched ground plane patterns are studied extensively in numerous publications [6]-[20]. Several different structures of this type are designed, fabricated and tested in this thesis. These designs are also simulated using Ansoft "Ensemble" software, showing a good agreement with measured results. The main problem with circular etched patterns is the lack of an equivalent circuit model, making the design a long process of trial and error, using a full wave simulator, such as "Ensemble". For the purpose of finding a relatively simple equivalent circuit model, the rectangular etched pattern is proposed and investigated in this thesis. The obtained models are analyzed with a program written in Matlab, and the results compared with the "Ensemble" simulations.

1.3 Thesis Outline

This thesis is divided into six chapters. Chapter one covered the introduction to microstrip transmission lines, photonic bandgap structures and the objectives of the thesis. The second chapter covers the background theory on transmission lines in general, and scattering parameters in microwave circuits. The basic formulas and considerations in microstrip transmission line design are given as well, followed by the background theory on photonic bandgap structures. The third chapter covers the microstrip lines with periodic contrast in the dielectric substrate. The effects of the dielectric contrast in this guided wave structure is compared with the effects in a dielectric stack structure without the conductors, where the waves propagate freely. Chapter four covers the microstrip transmission lines with periodic circular ground plane perforations. The effects of circular perforations are studied and compared with the photonic bandgap theory for the structures with periodic contrast in the dielectric material. The 2-port measurement results for several fabricated structures are presented and compared with the results obtained from a full wave simulator, Ansoft "Ensemble". Furthermore, the surface probe scanning results are presented as well in this chapter. Chapter five covers the microstrip transmission lines with periodic rectangular ground plane perforations. These structures are adequately modeled with cascaded equivalent circuits, making its analysis faster and easier. The results obtained from equivalent circuit model are compared with the results obtained from the full wave simulator. Finally, chapter six concludes the work completed, and provides some suggestions for the future work.

Chapter 2

Background Theory

This chapter is divided into four parts. The first part covers the basic transmission line theory, followed by the second part covering the scattering parameters application in microwave circuits. The third part covers the microstrip lines in particular, while the final part reviews the photonic bandgap theory for one-dimensional periodic contrasting dielectric layers, with a short subsection reviewing two-dimensional PBG's.

2.1 Transmission Line Theory

A transmission line in general is made of two or more conducting strips or wires, separated by a dielectric material, and it supports propagation of one or more guided wave modes along its axis. The dominant mode of operation can be assumed to be the quasi-TEM mode, where both electric and magnetic fields are transverse to the direction of propagation. Under this assumption, and when a transmission line is used for signals with wavelengths comparable to the length of the line, a distributed equivalent circuit transmission line model can be used to analyze the circuit variables, as shown in Fig. 2.1. In this model, the line series inductance L, parallel capacitance C, series conductor resistance R and parallel dielectric conductance G are expressed in per unit length values, rather than the lumped ones. The transmission line can be considered to be a cascaded connection of infinitesimal length segments, where the electrical element values in each

segment are obtained by multiplying per unit length values with the infinitesimal length Δz.

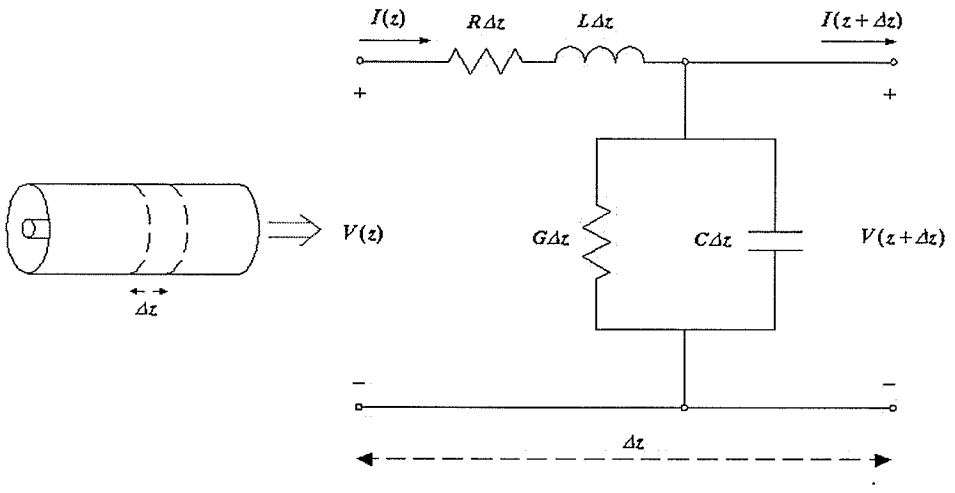

Fig. 2.1 Schematic of an infinitesimal segment in distributed transmission line model

After applying the circuit theory to such a segment, the resulting set of two second order differential equations, and their homogenous solution expressions for the voltage and current along the line are given by [3]:

$$\frac{d^2V(z)}{dz^2} - \gamma^2 V(z) = 0 \qquad (2.1\_a)$$

$$\frac{d^2I(z)}{dz^2} - \gamma^2 I(z) = 0 \qquad (2.1\_b)$$

$$V(z) = V_0^+ e^{-\gamma z} + V_0^- e^{+\gamma z} \qquad (2.1\_c)$$

$$I(z) = I_0^+ e^{-\gamma z} + I_0^- e^{+\gamma z} \qquad (2.1\_d)$$

where for the assumed frequency of operation, V and I are the total voltage and current phasors respectively, (V_0^+, I_0^+) are forward and (V_0^-, I_0^-) backward voltage and current incident traveling waves, and finally, γ is the propagation constant, given by [3]:

$$\gamma = \sqrt{(R + j\omega L)(G + j\omega C)} = \alpha + j\beta \qquad (2.2)$$

where α and β are the attenuation and phase constant, respectively. The propagation constant is one of the main parameters characterizing a transmission line. In the lossless case, (i.e. $\alpha = 0$) the propagation constant is purely imaginary, and it is determined by the phase constant β, given by:

$$\beta = \frac{2\pi}{\lambda} = \frac{\omega}{u} = \omega\sqrt{LC} = \frac{\omega}{c}\sqrt{\varepsilon_e} \qquad (2.3)$$

where ε_e is the effective dielectric permittivity used in case of lossless dielectric substrates, ω is the signal angular frequency, c is the speed of light in vacuum or air, u is the speed of propagation along the line and finally, λ is the wavelength at the signal frequency. The phase constant β represents the rate of signal phase change. Furthermore, if L and C are uniform in z direction and frequency independent, there will be no dispersion either (i.e. different frequency signal will not have different phase constants). The transmission line structures with higher effective dielectric permittivity values ε_e will have a slower wave propagation speed $u = c/\sqrt{\varepsilon_e}$. The next important property of a transmission line is its characteristic impedance, given by [3]:

$$Z_c = \frac{V_0^+}{I_0^+} = \sqrt{\frac{R + j\omega L}{G + j\omega C}} \cong \sqrt{\frac{L}{C}} \qquad (2.4)$$

The characteristic impedance is defined, as the incident wave voltage to current ratio and therefore is independent of the line length. Obviously, for the lossless case approximation in (2.4), the characteristic impedance is purely real (i.e. the incident voltage and current are in phase).

The diagram in Fig. 2.2 shows an impedance terminated transmission line along with the terminal sources specifying the incident (V_0^+) and reflected (V_0^-) voltage waves, which impose 2 boundary conditions for differential equations (2.1_a) and (2.1_b).

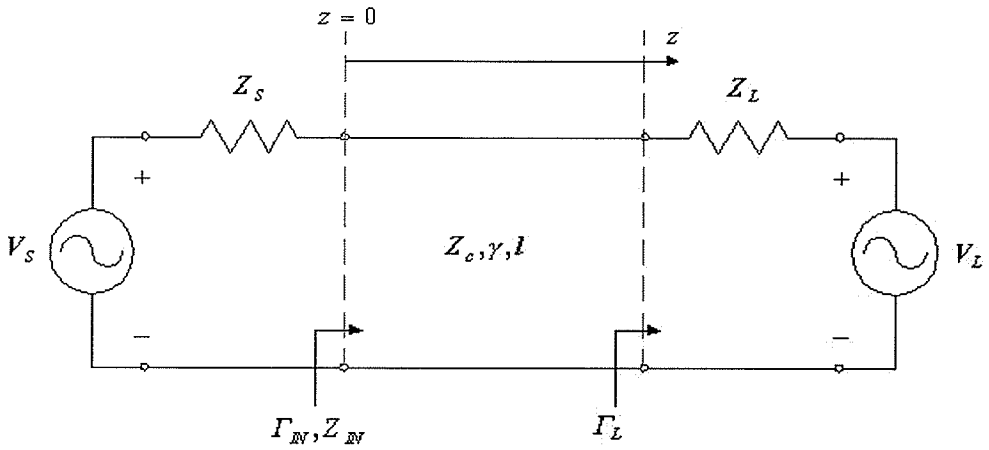

Fig. 2.2 Diagram of a finite length transmission line with imposed boundary conditions

Assuming a passive load (V_L=0), a given source voltage V_S and load Z_L, the reflection coefficient at the load is defined as [3]:

$$\Gamma_L = \frac{V_0^-}{V_0^+} = \frac{Z_L - Z_c}{Z_L + Z_c} \qquad (2.5)$$

Clearly, an open ($Z_L \to \infty$) or short (Z_L=0) circuit termination will result in a total reflection of the incident signal ($\Gamma_L = \pm 1$). The total impedance at the input of the line Z_{IN}, and the corresponding reflection coefficient Γ_{IN}, are given by [3]:

$$Z_{IN} = Z_c \frac{1+\Gamma_L e^{-j2\beta l}}{1-\Gamma_L e^{-j2\beta l}} \qquad (2.6\_a) \qquad \Gamma_{IN} = \frac{Z_{IN} - Z_S}{Z_{IN} + Z_S} \qquad (2.6\_b)$$

In summary, a distributed equivalent circuit model of a transmission line is completely characterized by its length *l*, its characteristic impedance Z_c, and its propagation constant γ, consisting of the phase constant β, and for a lossy line, the attenuation constant α.

2.2 Scattering Parameters

In microwave circuits, voltages and currents are rarely measured directly. Instead, a scattering parameter description is commonly used, which define a circuit in terms of incident and reflected power waves at its ports. In this thesis, only one-dimensional circuits are examined, which can be represented as 2-port networks, such as the one illustrated in Fig. 2.3. For each port of a network, the inward ***a*** and the outward ***b*** power waves are defined [4]:

$$a \equiv \frac{V^+}{\sqrt{Z_0}} \qquad b \equiv \frac{V^-}{\sqrt{Z_0}} \qquad (2.7)$$

where Z_0 is the normalizing impedance, which is usually the system impedance.

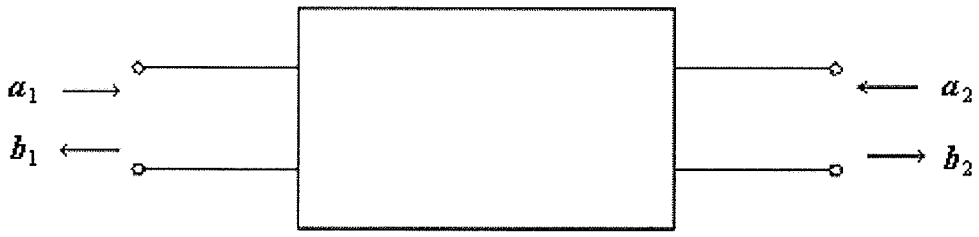

Fig. 2.3 Schematic of a 2-port network

These waves represent normalized incident and reflected power waves at a given port. In case of the normalized impedance being the same for all ports, the power waves also represent the incident and reflected voltages. The sum of the two power waves gives the total normalized voltage at the port, while the difference between the incident and reflected power wave gives the total current flowing into the port. Since the units of power waves are given in square root of Watts, the difference of the squares of the incident and reflected power waves at a port gives the total power going into the port [4]:

$$P_{in} = |\boldsymbol{a}|^2 - |\boldsymbol{b}|^2 = \frac{|V^+|^2}{Z_0} - \frac{|V^-|^2}{Z_0} \qquad (2.8)$$

The ratio of the reflected and the incident power wave at a port gives the reflection coefficient Γ, given there is no signal flow into other ports. A network can be completely characterized by its scattering parameters, which establish the relationships between the corresponding outward and inward power waves. This relationship, written in a matrix form for a 2-port network is given by [4]:

$$\begin{bmatrix} b_1 \\ b_2 \end{bmatrix} = \begin{bmatrix} S_{11} & S_{12} \\ S_{21} & S_{22} \end{bmatrix} \begin{bmatrix} a_1 \\ a_2 \end{bmatrix} \qquad (2.9)$$

From the matrix equation (2.9), it is evident that S_{11} represents the ratio of the reflected and the incident wave at the input port, when the output port is match terminated (i.e. the wave reflected by the output $a_2 = 0$). Similarly, S_{21} represents the ratio of the wave transmitted to the output port and the incident wave at the input, when the output port is match terminated:

$$S_{11} = \left.\frac{b_1}{a_1}\right|_{a_2=0} \qquad S_{21} = \left.\frac{b_2}{a_1}\right|_{a_2=0} \qquad (2.10)$$

The other two coefficients of a 2-port network, namely S_{12} and S_{22}, can be obtained by match terminating the input port ($a_1 = 0$), and finding the corresponding ratios. In summary, the scattering parameters for a 2-port network are determined by applying a signal to one port at the time, match terminating the other one, and finally measuring or analytically solving for corresponding signal ratios. Once the scattering parameters are known and inserted into a network, from equation (2.9) one can determine all power waves at the ports.

When a network consists of cascaded elements, it is often challenging to analytically determine overall parameters. It is more convenient to determine the scattering parameters for individual elements first, and then algebraically determine the overall scattering matrix. This can be achieved by converting the scattering matrix of each

element to the corresponding transmission matrix, also known as ABCD matrix. Now the overall ABCD matrix can be found by multiplying the individual ABCD matrices. Finally, the overall ABCD matrix is converted to the corresponding scattering matrix of the overall network. The equations for ABCD to scattering matrix conversion for a network with N elements are given by [4]:

$$\begin{bmatrix} v_i \\ i_i \end{bmatrix} = \begin{bmatrix} A_i & B_i \\ C_i & D_i \end{bmatrix} \cdot \begin{bmatrix} v_{i+1} \\ -i_{i+1} \end{bmatrix} \qquad i = 1,2,...N \qquad (2.11\_a)$$

$$\begin{bmatrix} v_1 \\ i_1 \end{bmatrix} = \begin{bmatrix} A_1 & B_1 \\ C_1 & D_1 \end{bmatrix} \cdot \begin{bmatrix} A_2 & B_2 \\ C_2 & D_2 \end{bmatrix} \cdots \begin{bmatrix} A_N & B_N \\ C_N & D_N \end{bmatrix} \cdot \begin{bmatrix} v_{N+1} \\ -i_{N+1} \end{bmatrix} \qquad (2.11\_b)$$

$$\begin{bmatrix} A & B \\ C & D \end{bmatrix} = \begin{bmatrix} A_1 & B_1 \\ C_1 & D_1 \end{bmatrix} \cdot \begin{bmatrix} A_2 & B_2 \\ C_2 & D_2 \end{bmatrix} \cdots \begin{bmatrix} A_N & B_N \\ C_N & D_N \end{bmatrix} \qquad (2.11\_c)$$

$$S_{11} = \frac{A + B - C - D}{A + B + C + D} \qquad (2.11\_d)$$

$$S_{21} = \frac{2}{A + B + C + D} \qquad (2.11\_e)$$

$$\begin{bmatrix} b_1 \\ b_{N+1} \end{bmatrix} = \begin{bmatrix} S_{11} & S_{12} \\ S_{21} & S_{22} \end{bmatrix} \cdot \begin{bmatrix} a_1 \\ a_{N+1} \end{bmatrix} \qquad (2.11\_f)$$

where index $N+1$ represents the output port of the overall network. A transmission line section of length l and arbitrary characteristic impedance Z_c, generally different from the system impedance Z_0, and propagation constant γ, is illustrated in Fig. 2.4.

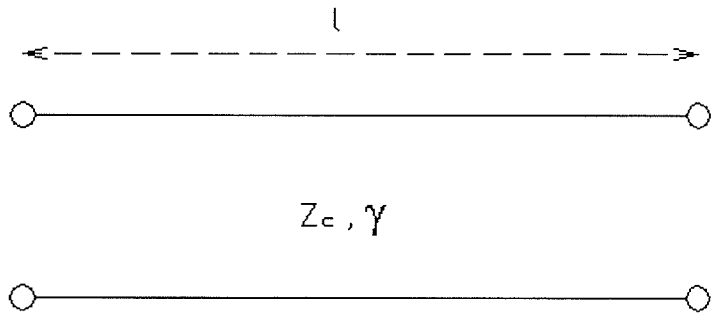

Fig. 2.4 Schematic of a transmission line section of length l, characteristic impedance Zc and propagation constant γ

The scattering parameters for this symmetric element are derived as:

$$S_{11} = \Gamma_1(1 - \frac{(1-\Gamma_1^2)e^{-2\gamma l}}{1-\Gamma_1^2 e^{-2\gamma l}}) \qquad (2.12\_a)$$

$$S_{21} = \frac{(1-\Gamma_1^2)e^{-\gamma l}}{1-\Gamma_1^2 e^{-2\gamma l}} \qquad (2.12\_b)$$

where $\Gamma_1 = \frac{Z_c - Z_0}{Z_c + Z_0}$ (2.12_c)

In this thesis, symmetrical one-dimensional structures modeled as cascaded transmission lines are studied. By examining Fig. 2.4, it is evident that the scattering matrix will be symmetric as well (i.e. $S_{22} = S_{11}$ and $S_{12} = S_{21}$). Therefore, the ABCD conversion equations for the other two parameters are omitted in (2.11). For a special case when the line impedance matches the system impedance (i.e. Γ_1=0), the scattering matrix and the corresponding ABCD matrix of this element are given by [4]:

$$\boldsymbol{S} = \begin{bmatrix} 0 & e^{-\gamma l} \\ e^{-\gamma l} & 0 \end{bmatrix} \qquad \boldsymbol{ABCD} = \begin{bmatrix} \cosh(\gamma l) & \sinh(\gamma l) \\ \sinh(\gamma l) & \cosh(\gamma l) \end{bmatrix} \qquad (2.13)$$

The general case for arbitrary line impedance Z_c can be alternatively modeled as a cascaded connection of a line that matches the system characteristic impedance, and the corresponding transformer step at each end of the line. The overall scattering matrix is then obtained by using the ABCD properties discussed earlier.

A transformer step from impedance Z_{o1} to Z_{o2} is characterized by [4]:

$$\boldsymbol{ABCD} = \begin{bmatrix} \sqrt{Z_{o2}/Z_{o1}} & 0 \\ 0 & \sqrt{Z_{o1}/Z_{o2}} \end{bmatrix} \qquad (2.14)$$

The lumped impedance elements will be included in circuit models in Chapter 5. A series element of normalized impedance z_s is characterized by [4]:

$$\boldsymbol{ABCD} = \begin{bmatrix} 1 & z_s \\ 0 & 1 \end{bmatrix} \qquad (2.15)$$

Finally, a shunt element of normalized admittance y_{sh} is characterized by [4]:

$$\boldsymbol{ABCD} = \begin{bmatrix} 1 & 0 \\ y_{sh} & 1 \end{bmatrix} \qquad (2.16)$$

2.3 Microstrip Transmission Lines

Microstrip transmission lines fall into the category of printed circuits. Fig. 2.5 illustrates printed circuit lines most commonly encountered in microwaves.

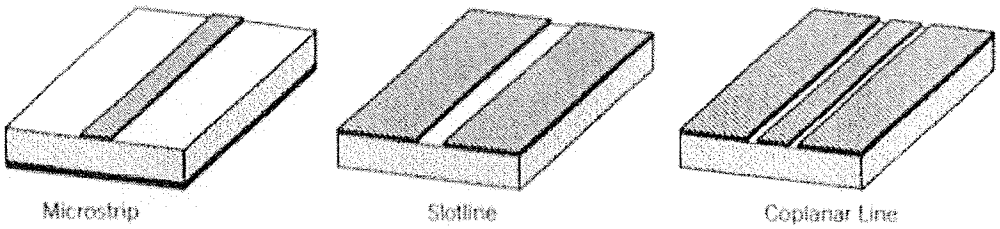

Fig. 2.5 Printed circuit transmission lines commonly used in microwaves [1]

As shown in the Figure, a microstrip line structure consists of a thin plate of low-loss insulating material called the substrate covered with metal completely on one side (i.e. ground plane) and partly on the other side where the strip conductor is printed. The microstrip transmission line is one of the most popular types of planar transmission lines primarily because it can be fabricated by photolithographic processes, and is easily integrated with other passive and active microwave devices [5]. The more detailed structure shown in Fig. 2.6 consists of a strip conductor of width w and thickness t, sitting on a dielectric substrate of height h and permittivity ε.

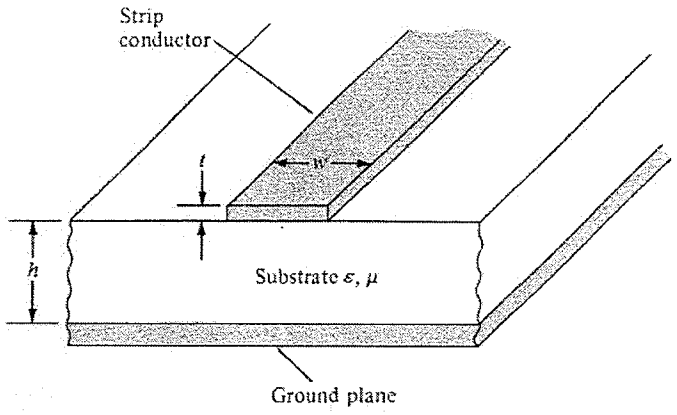

Fig. 2.6 Geometry of a microstrip transmission line [3]

For the microstrip structures studied in this thesis, the insulating substrate is a nonmagnetic material, having the magnetic permeability of free space μ_o, while its dielectric permittivity is related to free space permittivity by dielectric constant ε_r (i.e. $\varepsilon = \varepsilon_r \varepsilon_o$). Under the simple TEM assumption, the electric field for this structure can be visualized by solving an electrostatic boundary value problem for the cross section, which is uniform. This method will also be used in Chapter 5, to determine rectangular PBG structure parameters. If the ground plane is kept at a reference potential, while the strip conductor is kept at a constant potential V_o, the voltage at any point in the dielectric substrate and the surrounding air satisfies the Laplace equation:

$$\nabla^2 V = \frac{\partial^2 V}{\partial x^2} + \frac{\partial^2 V}{\partial y^2} = 0 \qquad (2.17)$$

where z coordinate is assumed along the axis of the transmission line. Once the potential V is determined, the vector electric field $\boldsymbol{E}$ can be found from $\boldsymbol{E} = -\nabla V$. The equation (2.17) needs to be solved by numerical methods, such as finite difference method. Once $\boldsymbol{E}$ is known, the per unit length parameter C can be determined by:

$$C = \frac{Q}{V_0} = \frac{\oiint_{S_1} \varepsilon \boldsymbol{E} \cdot \boldsymbol{dS}}{V_0} \qquad (2.18)$$

where the unit length integration surface S_1 encloses the strip conductor, and at each surface point only the $\boldsymbol{E}$ component normal to the surface is included in integration, along with the corresponding permittivity value ε.

Similarly, under the TEM assumption, a constant current I is assumed to flow through the line, and the magnetic vector potential $\boldsymbol{A}$ at any point in the cross section satisfies the vector Poisson's equation [3]:

$$\nabla^2 \boldsymbol{A} = -\mu_0 \boldsymbol{J} \qquad (2.19)$$

where $\boldsymbol{J}$ is the conductor current density. Since the constant current assumed flows only in the z direction, the vector equation (2.19) becomes a scalar equation with both $\boldsymbol{A}$ and $\boldsymbol{J}$ having the z component only. After the vector potential is solved for numerically, the vector magnetic field $\boldsymbol{H}$ can be found from $\boldsymbol{H} = \boldsymbol{B}/\mu = (\nabla \times \boldsymbol{A})/\mu$. The per unit length parameter L can be then found from:

$$L = \frac{\iint_{S_2} \mu \boldsymbol{H} \cdot d\boldsymbol{S}}{I} \qquad (2.20)$$

where the unit length integration surface S_2 is a cross section between the strip conductor and the ground plane along z direction, and at each surface point only the $\boldsymbol{H}$ component normal to the surface is included in integration, along with the corresponding permeability value μ. Once the per unit length parameters C and L are obtained from (2.18) and (2.20) respectively, one can determine the characteristic impedance Z_c for the transmission line from (2.4), while its effective permittivity can be found by rearranging (2.3), as $\varepsilon_e = c^2 LC$. Clearly, described procedure involves extensive numerical calculation, and in case of microstrip transmission lines, the empirical expressions for Z_c

and ε_e are available, as discussed later in this section. However, for structures studied in Chapter 5, such empirical formulas are not available, so the longer method will be used.

The general AC electromagnetic fields in a microstrip line are shown in Fig. 2.7.

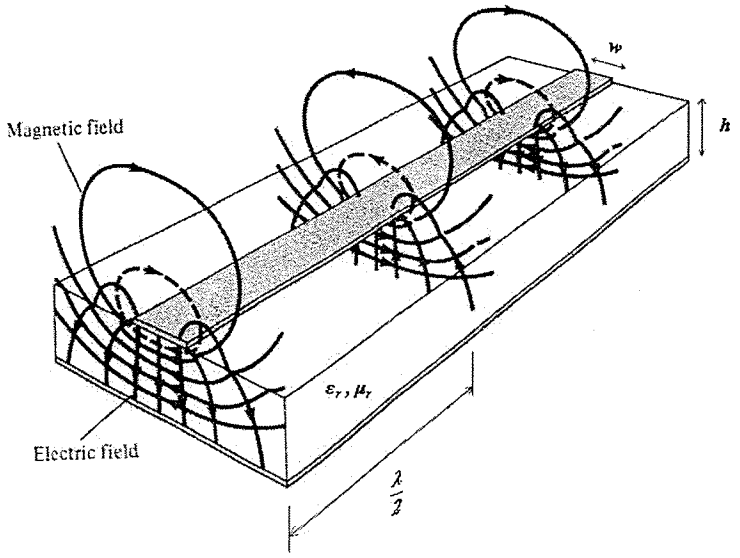

Fig. 2.7 Electric and magnetic fields in a microstrip line [3]

In this general case, both electric and magnetic fields experience the change in angle at the air to dielectric interface. When the substrate is a nonmagnetic material, only the electric field will experience the change in angle at the interface. Due to the boundary conditions, the tangential component of the electric field is continuous, while the normal component in the substrate is scaled down by a factor of the relative dielectric constant value ε_r. Since the fields in a microstrip transmission line are present both in the dielectric substrate and the air region, the concept of the effective dielectric permittivity is introduced. The effective permittivity value for a microstrip line can be estimated by empirical expressions, such as [5]:

$$\varepsilon_e = \frac{\varepsilon_r + 1}{2} + \frac{\varepsilon_r - 1}{2}\left(1 + \frac{12h}{w}\right)^{-\frac{1}{2}} \qquad 1 < \varepsilon_e < \varepsilon_r \qquad (2.21)$$

The effective permittivity value falls in between the dielectric constant of the substrate and the one of the air. As discussed in the background section 2.1, the effective permittivity value determines the signal speed of propagation, as per $u = c/\sqrt{\varepsilon_e}$. In reality, this approximation is valid only for lower frequencies, where the fields are close to being purely transversal to the direction of propagation (quasi-TEM approximation). The fields in the air region tend to propagate faster then the ones in the substrate. At the same time, the fields have to stay continuous at the dielectric to air interface. These effects result in the dominant mode deviating from its quasi-TEM approximation at higher frequencies. This effect is illustrated in Fig. 2.8.

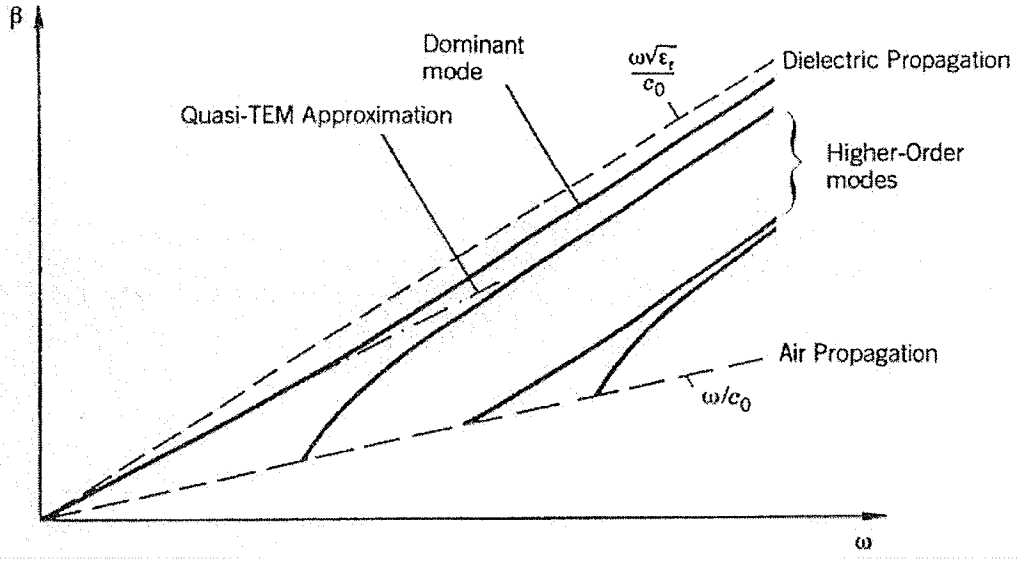

Fig. 2.8 Dispersion diagram of a microstrip line [1]

Obviously from Fig. 2.8, the propagation constant β of the dominant mode is not a linear function of frequency, except at the low frequency end of the range. At higher frequencies, the fields tend to concentrate more in the dielectric region, under the strip line. Consequently, the effective permittivity is increased towards the dielectric constant of the substrate. Even though the longitudinal field component of the dominant mode increases with frequency, the use of quasi-TEM mode can be somewhat extended by defining a frequency-dependent effective permittivity. Higher order modes will only propagate at very high frequencies ($w > \lambda/2$) and are usually ignored except at discontinuities.

The other important property of a transmission line, its characteristic impedance Z_c, can be approximated empirically by [5]:

$$Z_c = \frac{60}{\sqrt{\varepsilon_e}} \ln\left(\frac{8h}{w} + \frac{w}{4h}\right) \qquad \frac{w}{h} \le 1 \qquad (2.22\_a)$$

$$Z_c = \frac{120\pi}{\sqrt{\varepsilon_e}\left[\frac{w}{h} + 1.393 + 0.667 \ln\left(\frac{w}{h} + 1.444\right)\right]} \qquad \frac{w}{h} \ge 1 \qquad (2.22\_b)$$

In the empirical expressions for the effective permittivity (2.21) and the characteristic impedance (2.22), the strip conductor thickness is neglected. If the strip conductor thickness t is of the same order of magnitude as the substrate thickness h, it can be taken into account by an effective width given by [1]:

$$w_e = w + \frac{t}{\pi}\left[1 + \ln\left(\frac{2h}{t}\right)\right] \qquad w > h/2\pi \qquad (2.23\_a)$$

$$w_e = w + \frac{t}{\pi}[1 + \ln(\frac{4\pi w}{t})] \qquad 2t < w < h/2\pi \qquad (2.23\_b)$$

The empirical expressions for estimating Z_c and ε_e of a microstrip line are incorporated in "Linecalc" software application, which is used in this thesis.

The different types of waves that may be excited in microstrip structures are illustrated in Fig. 2.9.

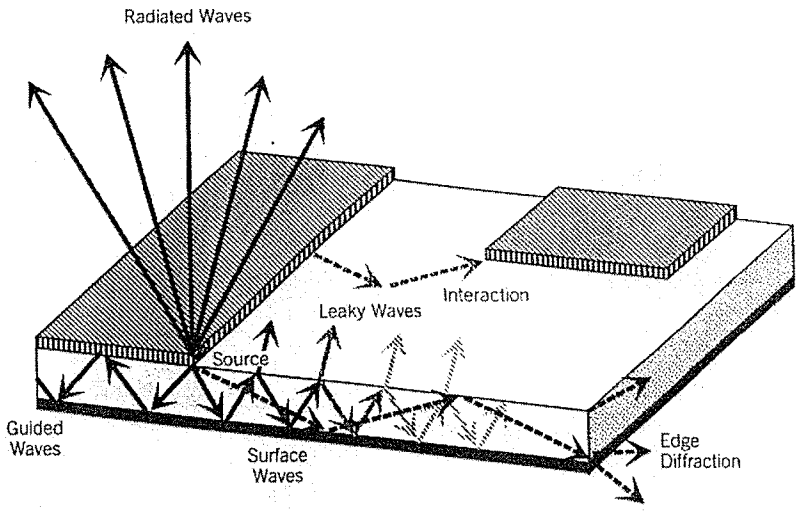

Fig. 2.9 Wave types in a microstrip structure [1]

A point source placed at the edge a microstrip due to an imposed source or discontinuity is considered in Fig. 2.9. The waves transmitted toward the open space above the line, are called radiated waves. They are required for the antenna operation, while they are unwanted for transmission lines as they produce signal leakage. The radiated waves are predominant when the substrate is thick and has a low permittivity. The waves transmitted into and guided by the top conductor are called guided waves. They may consist of the dominant quasi-TEM mode as well as higher order modes, as it was shown

in Fig. 2.8. They provide the normal operation of transmission lines and circuits. The guided waves are predominant when the substrate is thin and has a large permittivity. Other waves may be transmitted into the substrate away from the top conductor, and guided in the ground-dielectric slab. At the air-dielectric interface, they may be partly reflected (leaky waves), or totally reflected (surface waves). Leaky waves contribute to radiation, which makes them unwanted for the transmission lines. Surface waves have an incident angle larger than the critical angle at the dielectric to air interface and remain trapped within the dielectric substrate, where they propagate with small loss. The surface waves create apparent signal attenuation and also produce spurious coupling between circuit elements. The substrates with large permittivity have smaller critical angle of dielectric to air interface, thus supporting more surface waves. The lowest-order TM surface-wave mode can propagate at any frequency (i.e. it has no cutoff). However, its coupling to the mode of microstrip operation (quasi-TEM mode) is significant only when the signal frequency is close to the frequency of synchronism between the two modes [1]:

$$f_s = \frac{c \cdot \tan^{-1} \varepsilon_r}{\sqrt{2}\pi h \sqrt{\varepsilon_r - 1}} \qquad (2.24)$$

Theoretically, an infinite straight transmission line propagating the dominant mode does not radiate. However, as soon as some discontinuity appears along the line, higher-order radiating modes are excited. Approximately, these modes become significant for frequencies given by [1]:

$$f > 2.14 \times 10^6 \frac{\sqrt[4]{\varepsilon_r}}{h} \qquad (2.25)$$

The final frequency of concern in a microstrip design is the frequency of the first higher order mode, given by [1]:

$$f_c \cong \frac{c}{\sqrt{\varepsilon_r}(2w + 0.8h)} \qquad (2.26)$$

When the signal frequency exceeds this frequency, the first higher-order mode and the dominant mode can propagate with different velocities (Fig. 2.8). The signal transmitted to the end of the line is then a combination of the two modes, which results in distortion, because the two components are not in phase. In a microstrip transmission line design, it is recommended to calculate the three limiting frequencies (2.24), (2.25), (2.26), and then take the worst case (i.e. the lowest value). If the design frequency is higher than the lowest limiting frequency, a different substrate should be used (i.e. different height and/or dielectric constant) and the strip conductor width redesigned. These guidelines are followed for the structures studied in this thesis.

The final topic reviewed in this section deals with microstrip discontinuities. The discontinuities in a microstrip conductor come in the form of corners, gaps, open ends, steps in the conductor width and so on. The one-dimensional structures studied in Chapter 5 have axial discontinuities, and they are modeled with equivalent circuits. Discontinuities produce signal reflection, radiation, higher order modes and surface waves. Next to a discontinuity, the boundary conditions are not satisfied by the field components of the dominant mode alone. In fact, several modes must be present to satisfy

the field continuity requirements, thus making a discontinuity an apparent source of higher-order modes. A discontinuity in the form of conductor width step is of particular significance for this thesis. It is shown in Fig. 2.10, along with its equivalent circuit [1].

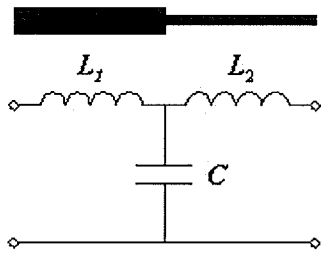

Fig. 2.10 Microstrip step equivalent circuit

Electric charges tend to pile up at the edges of a discontinuity, producing a local increase of charge on the conductor [1]. The resulting effect can be modeled with a lumped parallel capacitor in the equivalent circuit. A change in the cross section of the conductor modifies the distribution of the current, producing a local increase of the magnetic field. Magnetic energy is then stored in the higher-order modes, producing an inductive effect represented by a lumped inductance in the equivalent circuit, shown in Fig. 2.10. The equivalent circuit element values for a microstrip step discontinuity can be estimated by empirical expressions found in [1]. Once the equivalent circuit is included at the discontinuity, one can assume the presence of the dominant mode only.

2.4 Photonic Bandgap Structures

The general theory reviewed in this section will be used in Chapter 3 to develop a numerical method for the analysis of a specific one-dimensional PBG structure. Most of

the background material for this section is condensed from [2]. Photonic bandgap structures are periodic structures that prohibit the propagation of electromagnetic waves in certain directions for certain frequencies. They can be 1, 2 or 3-dimensional in nature, preventing the wave propagation in a single direction, a plane, or any spatial direction, respectively. The periodicity of the structure is often in the form of a periodic dielectric contrast, as shown in Fig. 2.11.

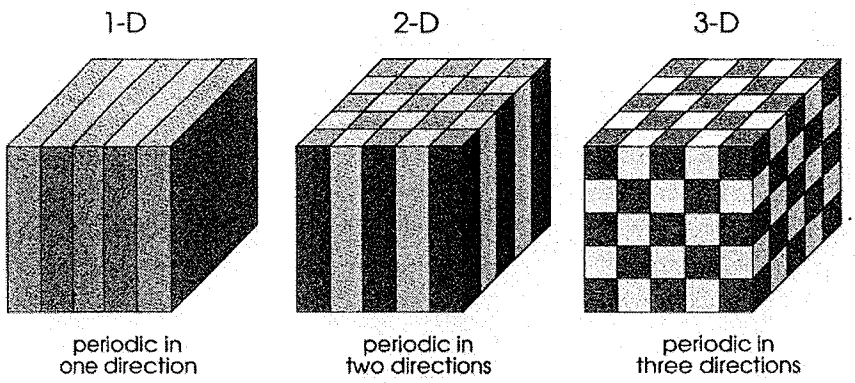

Fig. 2.11 1,2 and 3-dimensional photonic bandgap structures with periodic dielectric contrasts [2]

A photonic bandgap structure behaves as a stop band filter (i.e. the electromagnetic waves are transmitted through the structure, unless the wave frequency is within the stopband range, in which case they are completely reflected). The name "photonic" is used since the effect was first observed for the visible light electromagnetic waves, within so called "photonic crystals". There is an analogy between an electron propagating in a crystal lattice and an electromagnetic wave propagating in a "photonic crystal". A crystal is a periodic arrangement of atoms and molecules, therefore presenting a periodic potential to an electron propagating through it. As a result, the electrons are forbidden to propagate with certain energies in certain directions. In "photonic crystals", the periodic

"potential" is due to a periodic lattice of macroscopic dielectric media instead of atoms [2]. If the dielectric constants of the materials in the photonic crystal are different enough and the absorption of light by the material is minimum (i.e. low-loss dielectrics), then scattering at the interfaces can produce many of the same phenomena for *photons* (light modes) as the atomic potential does for *electrons* [2]. The controlling property of photonic crystals can be compared to the control of microwave propagation encountered in waveguides. A metallic waveguide only allows wave propagation along its axis, and for waves with frequencies above its cutoff frequency. These properties would be useful at frequencies outside the microwave range. However, the waves at visible light frequencies for instance are quickly dissipated in the metallic components of the waveguide, leaving the waveguide use confined to microwave frequency range only. Photonic crystals on the other hand, are scalable and applicable to a wider range of frequencies. We may construct a photonic crystal of a given geometry with millimeter dimensions for microwave control, or with micron dimensions for infrared control [2]. Therefore, the name "Electromagnetic Bandgap" Structures (i.e. EBG's) is also in use, in order to emphasize the applicability of the structures to a wide range of frequencies, not just the visible light.

All of macroscopic electromagnetism, including the propagation of waves in a photonic crystal, is governed by four macroscopic Maxwell equations. These equations, given in a point form, are [3]:

$$\nabla \cdot \mathbf{D} = \rho_v \qquad (2.27\_a) \qquad \nabla \cdot \mathbf{B} = 0 \qquad (2.27\_b)$$

$$\nabla \times \mathbf{E} = -\frac{\partial \mathbf{B}}{\partial t} \qquad (2.27\_c) \qquad\qquad \nabla \times \mathbf{H} = \mathbf{J} + \frac{\partial \mathbf{D}}{\partial t} \qquad (2.27\_d)$$

where (respectively) **E** and **H** are the macroscopic electric and magnetic vector fields, **D** and **B** are displacement and magnetic induction vector fields, while ρ_v and **J** are free charges and current densities. The PBG structures reviewed in this section (Fig. 2.11) can be regarded as a composite of regions of homogeneous dielectric material, with no free charges or currents (i.e. ρ_v=0 and **J**=*0).* Furthermore, several restrictions can be applied to the problem of analyzing these structures. First, we assume that the dielectric material is linear and isotropic, so that **E** and **D** vector fields are related by a scalar dielectric permittivity constant ε, while the **H** and **B** vector fields are related by a scalar magnetic permeability constant μ. Second, we ignore any explicit frequency dependence of the dielectric constant, and simply choose the value appropriate to the frequency range of the physical system we are considering. Finally, we focus only on lossless dielectric materials, which means that the dielectric constant is purely real. These restrictions make the PBG structures much easier to analyze, while keeping the results practically close to the exact values obtained in the experiments. After applying the listed restrictions to the general Maxwell equations (2.27), we end up with:

$$\nabla \cdot \varepsilon(\boldsymbol{r})\mathbf{E}(\boldsymbol{r},t) = 0 \qquad (2.28\_a) \qquad \nabla \cdot \mathbf{H}(\boldsymbol{r},t) = 0 \qquad (2.28\_b)$$

$$\nabla \times \mathbf{E}(\boldsymbol{r},t) = -\mu \frac{\partial \mathbf{H}(\boldsymbol{r},t)}{\partial t} \qquad (2.28\_c) \qquad \nabla \times \mathbf{H}(\boldsymbol{r},t) = \varepsilon(\boldsymbol{r}) \frac{\partial \mathbf{E}(\boldsymbol{r},t)}{\partial t} \qquad (2.28\_d)$$

where $\boldsymbol{r}$ is a position vector and t denotes time. The dielectric constant $\varepsilon(\boldsymbol{r})$ is a function of position in general and it is periodic in the cases shown in Fig. 2.11.In general, both **E** and **H** fields are complicated functions of time and space. However, since the Maxwell equations are linear, we can separate out the time dependence by expanding the fields into a set of harmonic modes (i.e. Fourier analysis). Therefore, we can restrict our analysis to the field patterns that are sinusoidal in time. For the mathematical convenience, it is common to use the complex valued quantities known as phasors in the calculations, keeping in mind that the physical quantities can be calculated by:

$$\mathbf{H}(\boldsymbol{r},t) = \mathbf{Re}\{\boldsymbol{H}(\boldsymbol{r})e^{j\omega t}\} \qquad (2.29\_a)$$

$$\mathbf{E}(\boldsymbol{r},t) = \mathbf{Re}\{\boldsymbol{E}(\boldsymbol{r})e^{j\omega t}\} \qquad (2.29\_b)$$

where $e^{j\omega t}$ is the assumed time dependence and $\boldsymbol{H(r)}$ and $\boldsymbol{E(r)}$ are complex valued magnetic and electric fields, respectively. The Maxwell equations for the observed problem (2.28) are then further simplified by considering the harmonic fields for a given frequency (2.29):

$$\nabla \cdot \varepsilon(\boldsymbol{r})\boldsymbol{E}(\boldsymbol{r}) = \rho_v = 0 \quad (2.30\_a) \qquad \nabla \cdot \boldsymbol{H}(\boldsymbol{r}) = 0 \quad (2.30\_b)$$

$$\nabla \times \boldsymbol{E}(\boldsymbol{r}) = -j\omega\mu\boldsymbol{H}(\boldsymbol{r}) \quad (2.30\_c) \qquad \nabla \times \boldsymbol{H}(\boldsymbol{r}) = j\omega\varepsilon(\boldsymbol{r})\boldsymbol{E}(\boldsymbol{r}) \quad (2.30\_d)$$

One way to decouple the equations (2.30) is to divide (2.30_d) by $\varepsilon(\boldsymbol{r})$ and then take the curl of both sides. After substituting the curl of $\boldsymbol{E}$ field from (2.30_c), we obtain the "master equation":

$$\nabla \times [\frac{1}{\varepsilon(\boldsymbol{r})} \nabla \times H(\boldsymbol{r})] = \omega^2 \mu \boldsymbol{E}(\boldsymbol{r}) \qquad (2.31)$$

Furthermore, if we consider the nonmagnetic materials only, the magnetic permeability for the entire structure will be equal to magnetic permeability of the free space μ_0. Finally, if the dielectric permittivity for each region is written as a product of its dielectric constant ε_r and the permittivity of the free space ε_0, the final form of the master equation for our problem becomes:

$$\nabla \times [\frac{1}{\varepsilon_r(\boldsymbol{r})} \nabla \times \boldsymbol{H}(\boldsymbol{r})] = (\frac{\omega}{c})^2 \boldsymbol{H}(\boldsymbol{r}) \qquad (2.32)$$

where c is the speed of light in free space, and it is given by [3]:

$$\boldsymbol{c} = \frac{1}{\sqrt{\varepsilon_0 \mu_0}} \qquad (2.33)$$

The dielectric constant $\varepsilon_r(\boldsymbol{r})$ is a function of position in general and for the cases shown in Fig. 2.11, it consists of periodic regions of constant permittivity. The master equation (2.32) in addition to the divergence equation (2.30_b) completely determines the harmonic magnetic field ***H(r)***. The divergence equations (2.30_a) and (2.30_b) also imply that the field configurations are built up of electromagnetic waves that are transverse (i.e. one of the field components are entirely in the plane that is orthogonal to the direction of propagation). Once the master equation (2.32) is solved for the magnetic

field mode ***H(r)*** for a given frequency, the corresponding electric field modes ***E(r)*** can be obtained from (2.30_d):

$$\boldsymbol{E}(\boldsymbol{r}) = \frac{1}{j\omega\varepsilon_0\varepsilon_r(\boldsymbol{r})}\nabla \times \boldsymbol{H}(\boldsymbol{r}) \qquad (2.34)$$

Finally, the complex fields ***H(r)*** and ***E(r)*** calculated from (2.32) and (2.34) respectively, can be substituted into equations (2.29), thus obtaining the time dependant physical field patterns for a given frequency.

The master equation (2.32) involves performing a series of operations on a function ***H(r)*** (i.e. taking its curl, dividing by the dielectric constant and taking the curl again). If ***H(r)*** is an allowable mode, the result of these operations will be the original function ***H(r)*** itself, multiplied by a constant (2.32). This situation is known as an eigenvalue problem in mathematical physics. The mentioned operations performed on a function ***H(r)*** can be identified as the linear differential operator Θ, and the equation (2.32) rewritten as:

$$\Theta\boldsymbol{H}(\boldsymbol{r}) = (\frac{\omega}{c})^2 \boldsymbol{H}(\boldsymbol{r}) \qquad (2.35)$$

The main reason for decoupling Maxwell equation in a way that we end up with a master equation in terms of the magnetic field ***H(r)*** only (2.32), lies in the fact that operator Θ is a *Hermitian* operator [2]. Had the master equation been in terms of the electric field ***E(r)*** instead, the same property of the consequent operator would not be observed. The Hermiticity of the operator Θ can be used to prove that the master equation

(2.32) has real and positive eigenvalues [2]. In other words, ω^2 is real and positive, therefore ω must be real as well. Furthermore, the Hermiticity of the operator Θ can be used to prove the following identity [2]:

$$(\omega_1^2 - \omega_2^2)(\boldsymbol{H}_2, \boldsymbol{H}_1) = (\omega_1^2 - \omega_2^2) \int \boldsymbol{H}_2^*(\boldsymbol{r}) \cdot \boldsymbol{H}_1(\boldsymbol{r}) d\boldsymbol{r} = 0 \qquad (2.36)$$

where $(\boldsymbol{H}_2, \boldsymbol{H}_1)$ is the inner product of the two modes. Equation (2.36) shows that for any two different modes ($\omega_1 \neq \omega_2$), their inner product must be equal to zero, in which case we say that $\boldsymbol{H}_1$ and $\boldsymbol{H}_2$ are *orthogonal* modes.

The electromagnetic variational theorem is very useful in studying the PBG structures. This theorem says that the lowest-energy (and therefore lowest-frequency) mode is the field pattern that minimizes the electromagnetic energy functional, given by [2]:

$$F_v(\boldsymbol{H}) = \frac{1}{2(\boldsymbol{H}, \boldsymbol{H})} \int \frac{1}{\varepsilon} |\, \omega \boldsymbol{D} \,|^2 \, d\boldsymbol{r} \qquad (2.37)$$

where the integration is performed over the space. In order to minimize this expression we can see that a harmonic mode will tend to concentrate its displacement field in regions of high dielectric constant. At the same time, the mode needs to remain orthogonal to the modes below it in frequency, according to the previous discussion.

The simplest PBG structure is a one-dimensional photonic crystal illustrated in Fig. 2.12, consisting of alternating layers of materials with different dielectric constants, namely ε_{r1} and ε_{r2}, which are repeated with period a, where the ε_{r1} layer is $d_1 a$ wide.

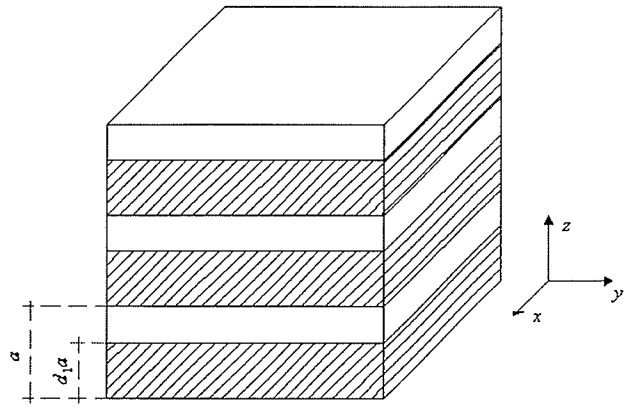

Fig. 2.12 A multilayer film structure (1-D photonic crystal)

This theoretically infinite multilayer film, acts as a perfect "mirror" for electromagnetic waves within a sharply defined gap. The traditional electromagnetic approach to the analysis of this system is to consider multiple reflections that take place at each interface. The special case to consider is when the periodical spacing a shown in the Figure, is such that a harmonic wave undergoes a phase change of 180° as it travels the distance a. Intuitively, we can expect that the scattered waves will add destructively within the photonic crystal. This will result in the total reflection of a harmonic wave with frequency that satisfies:

$$\beta a = \frac{\omega}{u} a = \frac{2\pi f}{c} \sqrt{\varepsilon_e}\, a = \pi \tag{2.38}$$

From this expression, the frequency that is intuitively expected to be within the stop band is given by:

$$f = \frac{c}{2a\sqrt{\varepsilon_e}} = \frac{c}{2a(d_1\sqrt{\varepsilon_{r1}} + (1-d_1)\sqrt{\varepsilon_{r2}})} \tag{2.39}$$

where ε_e is the effective dielectric permittivity. The right hand side of (2.39) involves the ε_e estimate valid at low frequencies only, as it will be discussed later.

In order to solve for the modes exactly, we need to make use of the discrete translational symmetry of this structure, which is illustrated in Fig. 2.13 below.

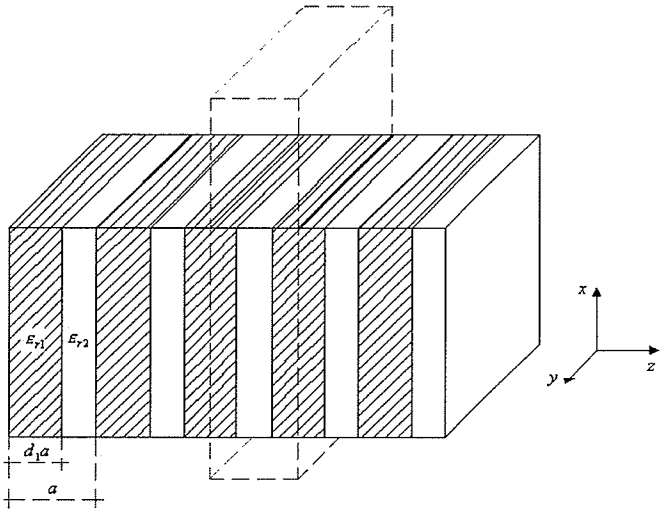

Fig. 2.13 Dielectric structure with a discrete translational symmetry

The theoretically infinite structure shown in Fig 2.13 is invariant under translations in the z direction only for distances that are a multiple of some fixed step length, which is the *lattice constant a*. The dielectric unit being periodically repeated is highlighted in the Figure, and it is known as the *unit cell*. In this example, the unit cell is a xy-slab of dielectric material with width a in the z direction. It can be shown, that the discrete periodicity in the z direction leads to a z-dependence for magnetic field $\boldsymbol{H(z)}$ that is simply the product of a plane wave with a z-periodic function $\boldsymbol{u}_{k_z}$ [2]:

$$\boldsymbol{H}(...,z,...) \propto e^{jk_z z} \cdot \boldsymbol{u}_{k_z}(z,...) \qquad (2.40)$$

This is known as *Bloch's theorem*, and the form of equation (2.40) is known as a *Bloch state*. The resulting field pattern can be thought of as a plane wave, as it would be in free space, but modulated by a periodic function $\boldsymbol{u}_{k_z}(z)$. Since the wave vector $\boldsymbol{k}_z$ is periodic with the period $2\pi/a$, we only consider the wave vector to exist in the range $(-\pi/a < \boldsymbol{k}_z \leq \pi/a)$. This region of important, non-redundant values of $\boldsymbol{k}_z$ is called the *Brillouin zone*. In order to solve for the periodic function $\boldsymbol{u}_k(z)$, the Bloch state (2.40) needs to be inserted into the master equation (2.32) and solved, subject to the periodic boundary condition:

$$\boldsymbol{u}_{k_z}(z) = \boldsymbol{u}_{k_z}(z + ma) \quad , \quad m \in I \qquad (2.41)$$

Because of this periodic boundary condition, the eigenvalue problem can be regarded as being restricted to a single unit cell of the photonic crystal (Fig. 2.13). It is known from mathematics that restricting an eigenvalue problem to a finite volume leads to a discrete spectrum of eigenvalues. An analogous example in quantum mechanics would be an electron confined to a "well", which resulted in discrete spectrum of allowable energy states. In our problem, for each value of wave number $\boldsymbol{k}$, it is expected to find an infinite set of modes with discretely spaced frequencies, labeled with the band index n. Furthermore, we can expect the frequency of each band for given $\boldsymbol{k}$, to vary continuously as $\boldsymbol{k}$ varies. Therefore, the modes of a photonic crystal are a family of continuous

functions $\omega_n(\boldsymbol{k})$ separated by the frequency bandgaps and indexed in order of increasing frequency.

In order to calculate the band structure functions $\omega_n(\boldsymbol{k})$, even for a simple multilayer film (Fig. 2.12), the master equation (2.32) needs to be solved numerically. The solutions have a form of Bloch states (2.40), and subject to the periodic boundary condition (2.41). The numerical solution involves a complicated iterative minimization technique for each value of the wave number $\boldsymbol{k}$. The band structure functions for three multilayer films with different dielectric constants are solved for in [2] and shown in Fig. 2.14 below.

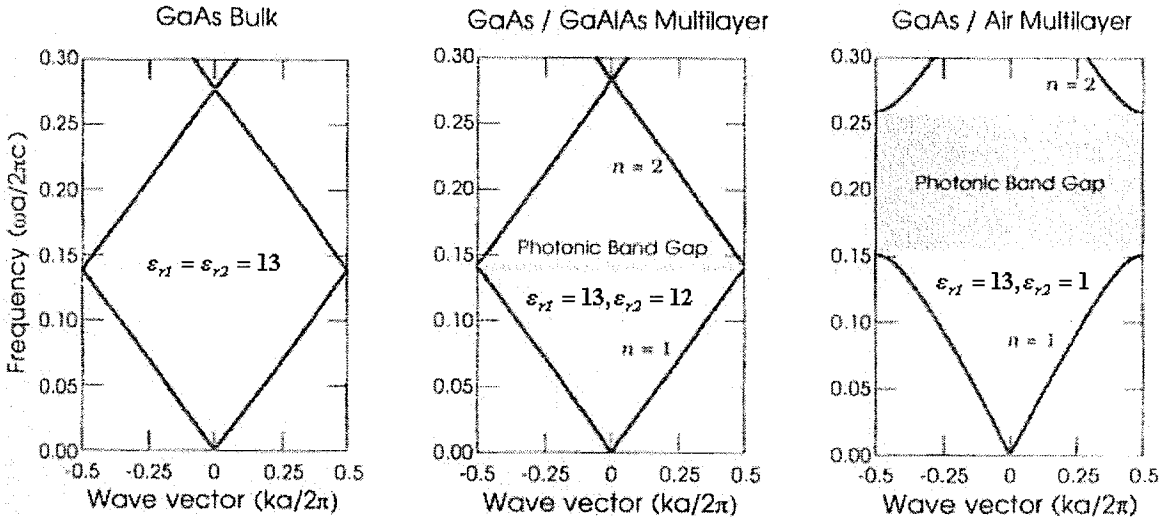

Fig. 2.14 Photonic band structures for 3 different multilayer films with the same layer widths d=a/2 [2]

Each band structure is calculated for the films having the contrasting layers of the same width *a/2*, along the axis of propagation. The dimensions in all three plots are scaled, making them universal for any lattice dimension *a*. The left hand side plot represents the case when all of the layers have the same dielectric constant $\varepsilon_r = 13$, so that the medium

is homogeneous. The medium is artificially assigned a periodicity of a, and the frequency spectrum is just a "light-line" given by:

$$\omega(k) = \frac{ck}{\sqrt{\varepsilon_r}} \qquad (2.42)$$

The speed of propagation in (2.42) is just the speed of light in free space reduced by a factor of square root of the medium dielectric constant. As discussed previously, the wave number k is uniquely defined within its Brillouin zone, which is represented by light-lines confinement within the zone edges (Fig. 2.14). The center plot in the Figure represents the nearly uniform case, where layers have a slight dielectric contrast, namely $\varepsilon_{r1} = 13$ and $\varepsilon_{r2} = 12$. This configuration introduces a small frequency gap, in which no mode can exist, regardless of its wave number k. Such a gap is called photonic bandgap (PBG) and it is shown in the Figure. The right hand side plot represents the case of increased dielectric contrasts in the layers, namely $\varepsilon_{r1} = 13$ and $\varepsilon_{r2} = 1$. As a result, the bandgap widens considerably, as shown in the plot.

Mathematically, the gap shown in the two plots is just a consequence of solving the Maxwell equations for the given structures. The physical origin of the gap can be understood by considering the field mode profiles for the states immediately below (index n = 1) and above (n = 2) the gap. The modes in the multilayer film consist of forward and backward traveling waves. At the Brillouin zone edge ($k = \pi / a$), just below or above the frequency bandgap, the backward and forward traveling waves have the same magnitude within each layer. Therefore, the modes at the bandgap edges are

standing waves with a wavelength of $2a$, twice the crystal's lattice constant. Due to the symmetry of the unit cell about its center, the standing wave nodes have to be positioned either in each high-ε_r or in each low-ε_r, as shown in Fig. 2.15 (*a* and *b*, respectively). The Figure shows the standing wave electric field and power locations for the modes immediately below and above the gap, for the film with a slight dielectric contrast, namely $\varepsilon_{r1} = 13$ and $\varepsilon_{r2} = 12$.

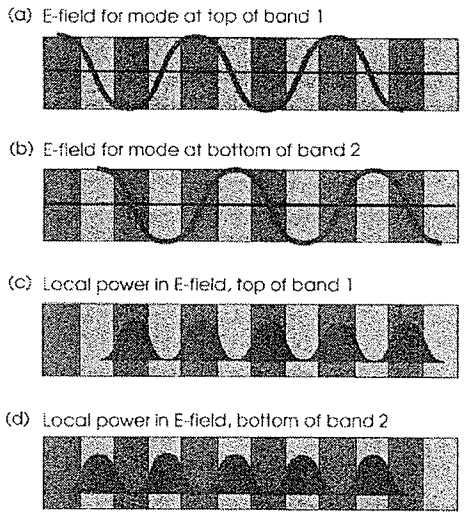

Fig. 2.15 Electric field standing wave positioning in a multilayer film ($\varepsilon_{r1} = 13$ *and* $\varepsilon_{r2} = 12$) [2]

According to the *electromagnetic variational theorem* discussed earlier, the low-frequency modes concentrate their energy in the high-ε_r region, while the high-frequency modes concentrate their energy in the low-ε_r regions. The standing wave mode centered in the low-ε_r region needs to be higher in frequency than the mode centered in the high-ε_r region, in order to undergo the phase change required for

sustaining the standing wave pattern in the structure. The higher the dielectric contrast, the higher the increase in frequency has to be for the low-ε_r region mode. There lies the physical reason for a frequency gap between the two cases. Furthermore, since these two modes have the same wave number k, they also have to be orthogonal to each other, as discussed earlier.

In the case when the alternating film layers are not of the same width, the bandgap undergoes the shift in frequency as well as the change in size. For the case illustrated in Fig. 2.16, the low-ε_r region takes 80% of the periodic step (the width of ε_r=1 region is 0.8a), while the ε_r=13 regions takes 20% of the periodic step (0.8a).

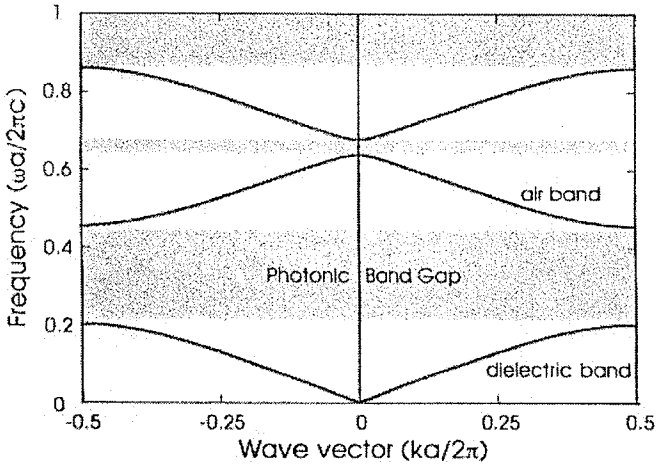

Fig. 2.16 The photonic band structure for a film with different layer widths (ε_r=13 layer is 0.2a wide, and ε_r=1 layer is 0.8a wide) [2]

For this specific case, the frequency gap has increased, as well as the center frequency of the gap (as expected, since now the effective permittivity is decreased, due to a larger contribution of low-ε_r region). The frequency band within the low-ε_r regions is

commonly referred to as the "air band", while the high-ε_r region band is known as the "dielectric band". In summary, the PBG for a multilayer film increases with the increase in the layer dielectric contrast, as well as with the increase in the proportion of the low-ε_r region, within the specified film periodicity.

2.4.1 Two-Dimensional Photonic Bandgap Structures

Even though two-dimensional structures are not studied in this thesis, a short overview is presented to provide the PBG theory completion. A two dimensional photonic crystal has a rotational symmetry within a plane. One example of a two dimensional structure is a square lattice of dielectric columns, as shown in Fig. 2.17.

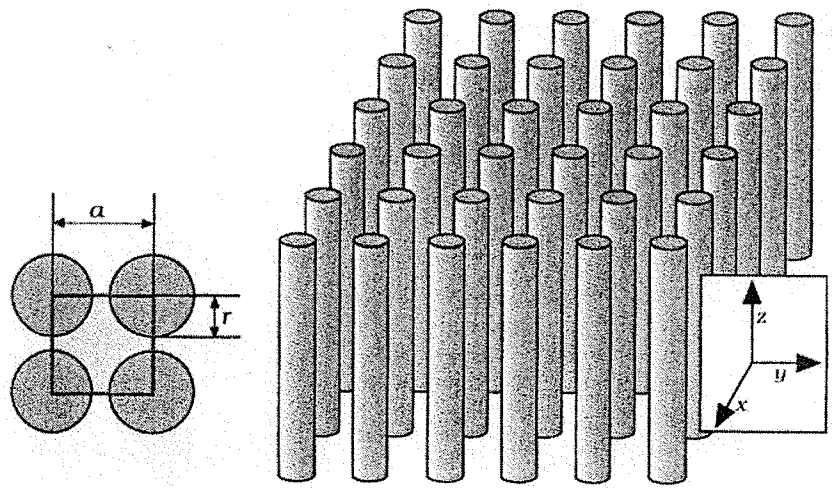

Fig. 2.17 A square lattice of dielectric columns with radius r and period a [2]

The irreducible Brillouin zone for this structure, where the wave vector $k_{\|}$ is non-redundant, is a shaded triangular wedge with 1/8 the area of the full Brillouin zone, as illustrated in Fig. 2.18.

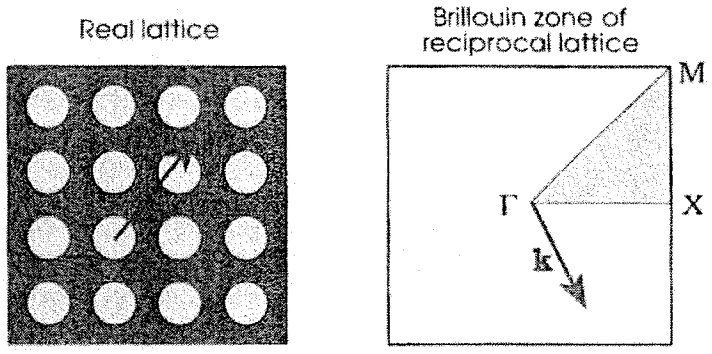

Fig. 2.18 The Brillouin zone of a square lattice [2]

Furthermore, for each wave vector we can distinguish two different polarizations. Transverse-electric (TE) modes have the $\boldsymbol{E}$ field in the plane and the $\boldsymbol{H}$ field normal to the plane, while the transverse-magnetic (TM) modes have the reverse situation. The band structures for these two modes can be quite different, and for a square lattice of dielectric columns (Fig. 2.17), the band structures are shown in Fig. 2.19. The dielectric columns used in the example have a dielectric constant of $\varepsilon_r = 8.9$ each, and the column radii take 20% of the lattice period ($r = 0.2a$).

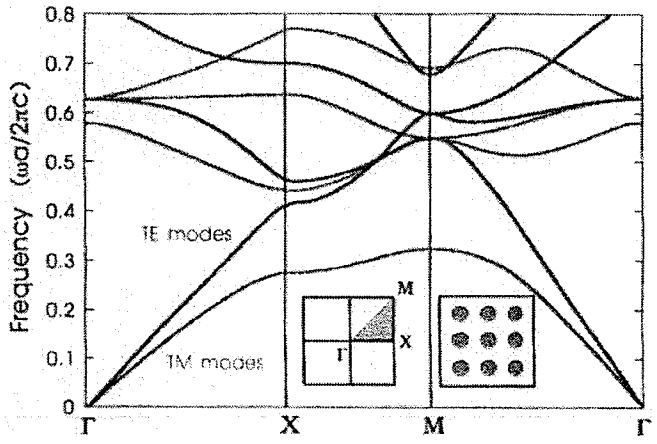

Fig. 2.19 The band structure for a square lattice of dielectric columns with $r = 0.2a$ and $\varepsilon_r = 8.9$ [2]

Clearly from Fig. 2.19, this particular photonic crystal has a complete band gap for the TM modes, but not for the TE modes. The main reason for this fact is that the lowest TM mode is strongly concentrated in the dielectric region. On the other hand, the next order (air-band) TM mode has a very small concentration in the dielectric region. This difference in the energy distribution of consecutive modes is responsible for the large TM photonic bandgap. The region concentrations for the TE modes do not contrast as strongly, resulting in smaller bandgaps for certain directions of propagation, and no bandgap at all for other directions (Fig. 2.19).

2.5 Conclusion

This chapter covered the background theory on transmission lines along with the scattering parameters used for the analysis of microwave circuits. Furthermore, the microstrip transmission lines in particular are covered, including the considerations and formulas needed for its design. Finally, the 1 and 2-dimensional PBG structures in contrasting dielectric media are covered, with detailed physical interpretations. The theory covered in this chapter will provide the references needed for topics covered in the subsequent chapters, involving the combination of microstrip line, microwave circuit, and the photonic bandgap theory.

Chapter 3

Microstrip Transmission Lines with Periodic Dielectric Contrast in the Substrate

This chapter covers the microstrip transmission lines with the substrate in the form of dielectric layers, stacked along the line. The chapter is divided into 2 sections. A numerical method for localizing the bandgap frequency intervals in multilayer films is developed in the first section. An equivalent circuit model for microstrip transmission lines with multilayer substrates is developed in the second section, and the results from the two sections are compared.

3.1 Numerical PBG Localization in Multilayer Films

In the previous chapter, the multilayer dielectric film structure (Fig. 2.12) was presented. This structure acts as a stopband filter, for the waves with frequencies within the structure's photonic bandgap. The numerical techniques commonly used for calculating the band structures of a multilayer film are fairly complicated and time consuming. The technique used in [2] involves iterative minimization techniques for computing the set of discrete frequencies for each value of the wave number. The technique developed in this section calculates the discrete frequencies at the structure's bandgap edges only, rather than calculating the continuous band structure functions $\omega_n(k)$. This restriction simplifies the problem considerably, while still being able to

provide the most important characteristic of the structure, namely its bandgap frequency intervals.

As mentioned in the previous chapter, the problem of determining the electromagnetic fields in an infinitely long multilayer dielectric film can be restricted to the unit cell. The multilayer film structure is made of an infinite number of adjacent unit cells, as illustrated in Fig. 2.13. A unit cell for an arbitrary multilayer film is shown in the Figure 3.1.

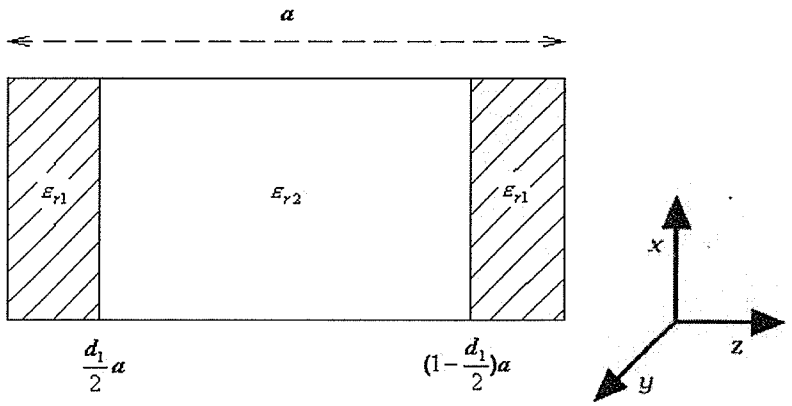

Fig. 3.1 The unit cell of a multilayer film

The alternating layers have dielectric constants of ε_{r1} and ε_{r2}, respectively. The fraction of the unit cell width a, occupied by the ε_{r1} layer is denoted as d_1, while the fraction occupied by the ε_{r2} layer is consequently $(1-d_1)$. The unit cell is positioned in such a way that the ε_{r1} layer is split into halves around the central ε_{r2} layer, as shown in the Figure. This way, the left and the right edges of the unit cell are positioned along the middle axis of consecutive ε_{r1} layers, while the middle axis of the unit cell coincides with the one of the ε_{r2} layer. This particular positioning introduces a symmetry that

simplifies the problem of solving for the field modes within the cell. The master equation (2.32) for a one dimensional problem becomes:

$$-\frac{\partial}{\partial z}[\frac{1}{\varepsilon_r(z)}\frac{\partial \boldsymbol{H}_y(z)}{\partial z}] = (\frac{\omega}{c})^2 \boldsymbol{H}_y(z) \qquad (3.1)$$

The coordinate system is chosen as shown in Fig. 3.1, while magnetic field modes $\boldsymbol{H}_y(z)$ are assumed to have the *y*-component only. This configuration dictates corresponding $\boldsymbol{E}_x(z)$ modes to be along the *x*-axis only, due to one of the Maxwell equations (2.30_d). Consequently, the waves propagate entirely along the *z*-axis. If the one dimensional master equation (3.1) is applied separately for the regions of constant ε_r, we obtain:

$$\frac{d^2 \boldsymbol{H}_y(z)}{dz^2} + \varepsilon_r(\frac{\omega}{c})^2 \boldsymbol{H}_y(z) = 0 \qquad (3.2)$$

having in mind that the magnetic field modes have a y-component only. The electric field modes can be obtained from equation (2.30_d), which can be written for the one dimensional case as:

$$\boldsymbol{E}_x(z) = -\frac{1}{j\omega\varepsilon_r}\frac{d\boldsymbol{H}_y(z)}{dz} \qquad (3.3)$$

assuming the electric field modes to be entirely along the *x*-axis, as discussed earlier. The second order differential equation (3.2) is a well known wave equation, with the propagation constant:

$$\gamma = j\beta = j\frac{\omega}{c}\sqrt{\varepsilon_r} \tag{3.4}$$

Therefore, the master equation solution within a region of constant ε_r is a sum of forward ($\boldsymbol{H}_{y0}^{+}$) and backward ($\boldsymbol{H}_{y0}^{-}$) traveling waves, with the phasor form given by:

$$\boldsymbol{H}_y(z) = \boldsymbol{H}_{y0}^{+} e^{-j\frac{\omega}{c}\sqrt{\varepsilon_r} z} + \boldsymbol{H}_{y0}^{-} e^{j\frac{\omega}{c}\sqrt{\varepsilon_r} z} \tag{3.5}$$

Having in mind that the physical fields can be obtained from phasors by using (2.29), the corresponding electric field modes in phasor form can be obtained from (3.3):

$$\boldsymbol{E}_x(z) = \frac{1}{c\varepsilon_0\sqrt{\varepsilon_r}}(\boldsymbol{H}_{y0}^{+} e^{-j\frac{\omega}{c}\sqrt{\varepsilon_r} z} - \boldsymbol{H}_{y0}^{-} e^{j\frac{\omega}{c}\sqrt{\varepsilon_r} z}) \tag{3.6}$$

As mentioned previously, the numerical technique being developed in this section calculates only the frequencies at the edges of bandgaps. From the discussion in section 2.4, we know that the modes at these special frequencies are standing waves, with their nodes positioned at the midpoints of either high-ε_r or low-ε_r regions. Furthermore, from Bloch's theorem (2.40) we know that the mode pattern is a plane wave, "modulated" with a periodic function *u(z)*, having the period of the unit cell width *a*. Therefore, the right hand side ε_{r1} region within the unit cell (Fig. 3.1) will have the same shape of the standing wave modes, as the left hand side ε_{r1} region. The lowest frequency for which this effect occurs is when the corresponding standing waves are out of phase by 180° (i.e.

the standing waves amplitudes are the negative of one another). Furthermore, since our solution is written in the form of forward and backward traveling waves (3.5), we have to think of the standing waves as a sum of the two direction traveling waves with the amplitudes that are complex conjugate of one another. Finally, we will assume that these amplitudes in the ε_{r1} region are purely real for the magnetic fields, and therefore equal for the forward and backward traveling waves. This particular assumption makes the magnetic standing wave nodes located in the ε_{r1} regions, while the electric field nodes are consequently located in the ε_{r2} regions, according to the equation (3.3). Having the above considerations in mind, the magnetic field modes for the three unit cell regions (Fig. 3.1) can be written as:

$$\boldsymbol{H}_{y1}(z) = \boldsymbol{H}_{y1}^{+}(e^{-j\frac{\omega}{c}\sqrt{\varepsilon_{r1}}z} + e^{j\frac{\omega}{c}\sqrt{\varepsilon_{r1}}z}) \qquad for\ (0 \le z < \frac{d_1}{2}a) \qquad (3.7\_a)$$

$$\boldsymbol{H}_{y2}(z) = \boldsymbol{H}_{y2}^{+}e^{-j\frac{\omega}{c}\sqrt{\varepsilon_{r2}}z} + \boldsymbol{H}_{y2}^{-}e^{j\frac{\omega}{c}\sqrt{\varepsilon_{r2}}z} \qquad for\ [\frac{d_1}{2}a \le z < (1-\frac{d_1}{2}a)] \qquad (3.7\_b)$$

$$\boldsymbol{H}_{y3}(z) = \mp\boldsymbol{H}_{y1}^{+}(e^{-j\frac{\omega}{c}\sqrt{\varepsilon_{r1}}(z-a)} + e^{j\frac{\omega}{c}\sqrt{\varepsilon_{r1}}(z-a)}) \quad for\ [(1-\frac{d_1}{2}a) \le z < a] \qquad (3.7\_c)$$

where the negative sign in the last equation (3.7_c) will yield a solution that is lower in frequency (i.e. the standing waves in the first and the third region are out of phase by 180°). The amplitude of the magnetic wave incident to the first region of the unit cell, namely $\boldsymbol{H}_{y1}^{+}$, is assumed purely real and given. Therefore, we are left with 2 unknowns to solve for, the central region magnetic wave amplitudes $\boldsymbol{H}_{y2}^{+}$ and $\boldsymbol{H}_{y2}^{-}$. As expected for a

standing wave, they will turn out to be complex conjugate values. For the situation described by (3.7), where the magnetic standing wave nodes are located in the ε_{r1} regions, the electric standing wave nodes will consequently be located in the ε_{r2} regions, and the corresponding waves are given by:

$$\boldsymbol{E}_{x1}(z) = \frac{1}{c\varepsilon_0\sqrt{\varepsilon_{r1}}}\boldsymbol{H}^{+}_{y1}(e^{-j\frac{\omega}{c}\sqrt{\varepsilon_{r1}}z} - e^{j\frac{\omega}{c}\sqrt{\varepsilon_{r1}}z}) \qquad for \quad (0 \le z < \frac{d_1}{2}a) \qquad (3.8\_a)$$

$$\boldsymbol{E}_{x2}(z) = \frac{1}{c\varepsilon_0\sqrt{\varepsilon_{r2}}}(\boldsymbol{H}^{+}_{y2}e^{-j\frac{\omega}{c}\sqrt{\varepsilon_{r2}}z} - \boldsymbol{H}^{+}_{y2}e^{j\frac{\omega}{c}\sqrt{\varepsilon_{r2}}z}) \qquad for \quad [\frac{d_1}{2}a \le z < (1-\frac{d_1}{2}a)] \qquad (3.8\_b)$$

$$\boldsymbol{E}_{x3}(z) = \mp\frac{1}{c\varepsilon_0\sqrt{\varepsilon_{r1}}}\boldsymbol{H}^{+}_{y1}(e^{-j\frac{\omega}{c}\sqrt{\varepsilon_{r1}}(z-a)} - e^{j\frac{\omega}{c}\sqrt{\varepsilon_{r1}}(z-a)}) \quad for \quad [(1-\frac{d_1}{2}a) \le z < a] \qquad (3.8\_c)$$

According to the boundary conditions, both the magnetic end the electric field tangential components have to be continuous at the dielectric interfaces. In our case, the electric and magnetic fields are entirely tangential to the interfaces, thus making the boundary conditions a matter of equating corresponding expressions given by (3.7) and (3.8). In order to satisfy the magnetic field continuity requirements at the two inner boundaries, the following set of equations needs to be solved:

$$\boldsymbol{H}_{y1}(\frac{d_1}{2}a) = \boldsymbol{H}_{y2}(\frac{d_1}{2}a) \qquad (3.9\_a)$$

$$\boldsymbol{H}_{y2}[(1-\frac{d_1}{2})a] = \boldsymbol{H}_{y3}[(1-\frac{d_1}{2})a] \qquad (3.9\_b)$$

In these equations, the functions $\boldsymbol{H}_{y1}$, $\boldsymbol{H}_{y2}$, and $\boldsymbol{H}_{y3}$ are the magnetic field expressions in the three regions, given by (3.7_a), (3.7_b) and (3.7_c), respectively. Similarly, the electric filed continuity requirements can be expressed as:

$$\boldsymbol{E}_{x1}(\frac{d_1}{2}a) = \boldsymbol{E}_{x2}(\frac{d_1}{2}a) \qquad (3.10\_a)$$

$$\boldsymbol{E}_{x2}[(1-\frac{d_1}{2})a] = \boldsymbol{E}_{x3}[(1-\frac{d_1}{2})a] \qquad (3.10\_b)$$

where $\boldsymbol{E}_{x1}$, $\boldsymbol{E}_{x2}$, and $\boldsymbol{E}_{x3}$ are the electric field expressions in the three regions, given by (3.8_a), (3.8_b) and (3.8_c), respectively. Both sets of equation, (3.9) and (3.10), have 2 unknowns, namely $\boldsymbol{H}_{y2}^{+}$ and $\boldsymbol{H}_{y2}^{-}$. For an arbitrary frequency, these two sets of equations will generally yield different solutions for the unknowns. This would violate the boundary conditions, thus making a solution valid only for those frequencies where both sets of equations yield the same solution.

The numerical technique developed in this chapter involves a frequency sweep, followed by the solution comparison from the two sets of equations. The frequencies for which the solutions coincide are recorded, and they are the bandgap edge frequencies, since they allow valid standing waves modes. If for example, the ε_{r1} regions are higher in dielectric constant than the ε_{r2} regions, according to (3.8), the electric standing wave nodes will be located in the regions of lower dielectric constant, namely ε_{r2}. Since the lowest energy mode has its electric field located in the regions of high dielectric constant, the numerical solution in this example will yield the higher band edge frequency. In order

to obtain the lower band edge frequency, while keeping the expressions (3.7) and (3.8) unchanged, the unit cell needs to be repositioned so that the low-ε_r regions surround the central high-ε_r region. Therefore, the electric standing wave nodes will be in the regions of high dielectric constant, yielding the lower band edge frequency. The resulting electromagnetic waves can be reconstructed for the original unit cell, by using the applicable symmetries.

A Matlab program implementing the described procedures was written. The program was tested for several examples presented in [2], with their band structure functions shown in Fig. 2.14 and Fig. 2.16 of the previous chapter, and a perfect agreement was obtained. For comparison purposes with the structure studied in section 3.2, a multilayer film of period a = 14 mm, with alternating dielectric layers of ε_{r1}=7.21 and ε_{r2}=1, is considered. The dielectric layer widths are w_1=9 *mm* and w_2=5 *mm*, respectively. The first frequency bandgap interval was found to be between f_1=4.11 *GHz* and f_2=5.75 *GHz*. $\boldsymbol{E}_x(z)$ and $\boldsymbol{H}_y(z)$ fields at these frequencies are shown in Fig. 3.2 and Fig. 3.3.

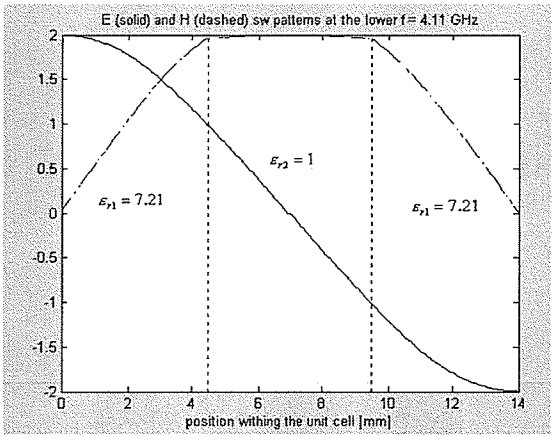

Fig. 3.2 Field patterns at the lower bandgap frequency f=4.11 GHz, for a=14mm, $w_1 = 9mm$, $w_2 = 5mm$, $\varepsilon_{r1} = 7.21$, $\varepsilon_{r2} = 1$

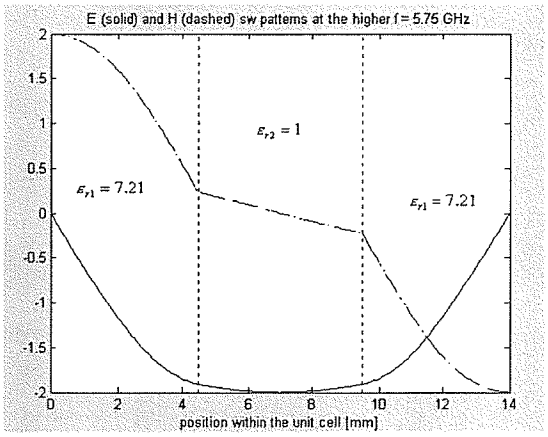

Fig. 3.3 Field patterns at the higher bandgap frequency f=5.75 GHz, for a=14mm, $w_1 = 9mm$, $w_2 = 5mm$, $\varepsilon_{r1} = 7.21$, $\varepsilon_{r2} = 1$

Clearly from Fig. 3.2 and 3.3, the phase difference between the first and the third regions is 180°. The electric field mode (solid line) is concentrated in the high-ε_r regions at the lower frequency f_1=4.11 *GHz*, while at the higher bandgap edge frequency f_2=5.75 *GHz*, the electric fields are mostly concentrated in the low-ε_r regions, which is in general agreement with Fig. 2.15. For the magnetic fields the opposite is true, due to their relationship to electric fields, expressed in (3.3).

At low frequencies the reflected waves can be ignored and the effective permittivity of a unit cell can be thought of as the relative permittivity of an equivalent homogeneous structure having the same length *a*, yielding the same phase shift, thus satisfying:

$$\frac{\omega}{c}\sqrt{\varepsilon_{r1}}d_1 a + \frac{\omega}{c}\sqrt{\varepsilon_{r2}}(1-d_1)a = \frac{\omega}{c}\sqrt{\varepsilon_e}a \qquad (3.11)$$

From this identity, the low frequency effective permittivity of this particular multilayer film is given by:

$$\varepsilon_e = (d_1\sqrt{\varepsilon_{r1}} + (1-d_1)\sqrt{\varepsilon_{r2}})^2 = 4.34 \qquad (3.12)$$

The corresponding frequency which would results in a 180° phase change of a traveling wave is calculated from (2.39):

$$f_c = \frac{c}{2a\sqrt{\varepsilon_e}} = 5.14GHz \qquad (3.13)$$

This frequency is within the bandgap as intuitively expected, and it does not coincide with the arithmetic mean of the band edge frequencies, which happens to be at 4.93 *GHz*.

3.2 Microstrip Lines with Multilayer Substrates

The multilayer dielectric film analyzed in the previous section behaves as a stopband filter for frequencies within the bandgap of the structure. Intuitively, we can expect the similar effect for a microstrip transmission line, when the homogeneous dielectric substrate is replaced with a multilayer substrate, as shown idealistically in Fig. 3.4.

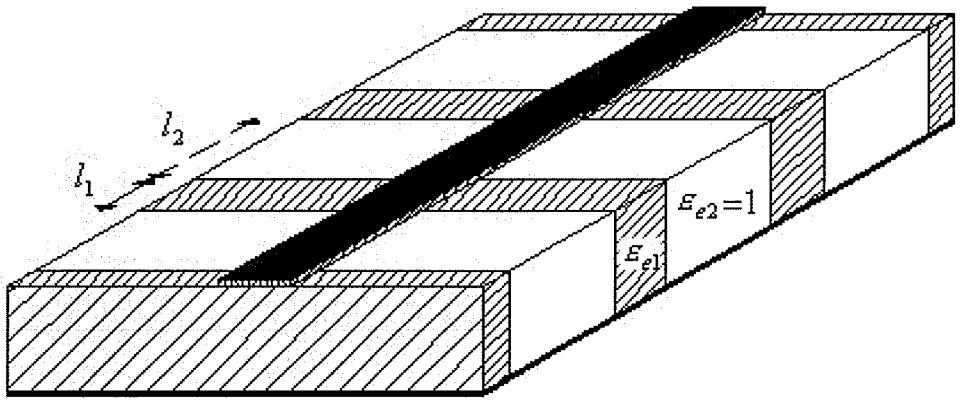

Fig. 3.4 Microstrip line with a multilayer dielectric substrate

Practically, the low permittivity ε_{e2} layers in Fig. 3.4 consist of a dense grid of air "filled" cylinders, drilled through the original homogeneous substrate. As discussed in section 2.3, the dominant mode of operation for a microstrip line is quasi-TEM mode, if the frequency of operation is low enough (2.24, 2.25 and 2.26). Under this assumption, there are no higher order modes in this analysis, and the electric and magnetic fields are considered to be transversal to the direction of propagation, while the speed of propagation is dictated by the effective permittivity, given by (2.21). Therefore, the structure shown in Fig. 3.4 can be regarded as a cascaded connection of transmission line segments with corresponding effective permittivity and characteristic impedance values. The next step would be to approximate this structure by the multilayer stack only, with the same dimensions. However, each layer's dielectric constant needs to be replaced by the effective permittivity of the corresponding cascaded transmission line. Finally, if the number of dielectric layers is large enough, we can apply the PBG theory for an infinitely long multilayer film, discussed in the previous section. The procedure of solving for the stopband of the structure shown in Fig. 3.4 is explained in an example.

The original microstrip line with the trace width w=0.554 *mm*, the substrate height h=0.635*mm* and uniform dielectric constant ε_{r1}=10.8 is considered first. The line characteristic impedance is found to be Z_{01}=50Ω, and the effective permittivity is ε_{e1}=7.21, implementing the equations (2.22) and (2.21), respectively. The sections of microstrip line with ideally air "filled" substrate as shown in Fig. 3.4 have the same strip width and substrate height, except that the dielectric constant now is $\varepsilon_{r2}=\varepsilon_{e2}$=1.

Implementing equations (2.22) and (2.21) again, the characteristic impedance of these sections is calculated to be Z_{02}=133.24 Ω. Furthermore, the substrate period a=14mm, where the higher effective permittivity layers (i.e. ε_{e1}=7.21) have a width w_1 = 9 mm and the air filled layers (ε_{e2}=1) have w_2=5 mm. This example matches the multilayer film example from the previous section exactly, and if the microstrip line structure is practically long enough (compared with the substrate period a), we can use the results obtained previously. Accordingly, we can say that for the microstrip structure in this example, the stopband interval is expected to fall between the lower bandgap edge frequency f_1=4.11GHz, and the higher bandgap edge frequency f_2=5.75 GHz.

In order to verify this claim, we can analyze the structure by applying the network theory discussed in section 2.2. The "unit cell" of this microstrip structure can be modeled as a cascaded connection of transmission lines with corresponding characteristic impedances and effective permittivities, as shown in Fig. 3.5.

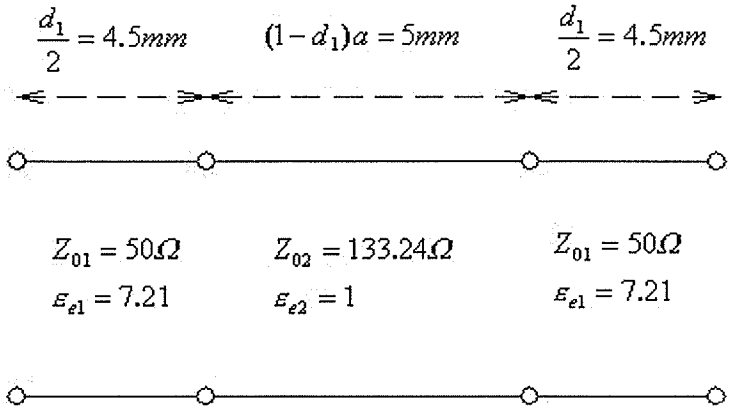

Fig. 3.5 Cascaded model of a multilayer substrate microstrip line unit cell with a=14 mm, d_1=64.28%, ε_{e1}=7.21, ε_{e2}=1, Z_{01}=50 Ω and Z_{02}=133.24 Ω

The unit cell of width a=14mm shown in Fig. 3.5, is repeated successively until the desired length of the line is reached. As discussed in section 2.2, a cascaded connection of circuit elements is best analyzed using the ABCD matrix parameters. The ABCD parameters are found for each cascaded segment, and the overall ABCD matrix is obtained by multiplication of individual matrices. The overall scattering parameters can be obtained from expressions (2.11_d) and (2.11_e).

In our example, the first and the third cascaded sections from Fig. 3.5 have Z_{01}=50Ω, ε_{e1}=7.21, and the length l_1=4.5 mm each. The middle section has Z_{02}=133.24 Ω, ε_{e2}=1 and the length l_2=5mm. The reference impedance is chosen to be 50Ω, therefore making the first and the third sections matched to the system impedance. These two sections of the cascaded model are therefore described by the following ABCD matrix:

$$\boldsymbol{ABCD}\_1 = \begin{bmatrix} \mathbf{cosh}(j\beta_1) & \mathbf{sinh}(j\beta_1) \\ \mathbf{sinh}(j\beta_1) & \mathbf{cosh}(j\beta_1) \end{bmatrix} \qquad (3.14\_a)$$

with $$\beta_1 = \frac{\omega}{c}\sqrt{\varepsilon_{e1}}\,l_1 \qquad (3.14\_b)$$

This model is valid for a lossless line only, just like the PBG theory covered is restricted to lossless dielectric media. The ABCD matrix for the middle section of the cascaded model has an expanded form, due to the transforming impedance elements, which make up for the characteristic impedance difference of the line. As discussed in section 2.2, the total ABCD matrix of this particular section is given by:

$$\boldsymbol{ABCD\_2} = \begin{bmatrix} \boldsymbol{n} & 0 \\ 0 & 1/\boldsymbol{n} \end{bmatrix} \begin{bmatrix} \mathbf{cosh}(j\beta_2) & \mathbf{sinh}(j\beta_2) \\ \mathbf{sinh}(j\beta_2) & \mathbf{cosh}(j\beta_2) \end{bmatrix} \begin{bmatrix} 1/\boldsymbol{n} & 0 \\ 0 & \boldsymbol{n} \end{bmatrix} \tag{3.15_a}$$

with $$\beta_2 = \frac{\omega}{c}\sqrt{\varepsilon_{e2}}\, l_2 \tag{3.15_b}$$

and $$n = \sqrt{\frac{Z_{02}}{Z_{01}}} \tag{3.15_c}$$

Now the overall ABCD matrices of the unit cell segment from Fig. 3.5 and the overall structure from Fig. 3.4, are given by the following expressions:

$$\boldsymbol{ABCD\_cell} = (\boldsymbol{ABCD\_1}) * (\boldsymbol{ABCD\_2}) * (\boldsymbol{ABCD\_1}) \tag{3.16_a}$$

$$\boldsymbol{ABCD\_structure} = (\boldsymbol{ABCD\_cell})^N \tag{3.16_b}$$

where N is the number of unit cell segments in the overall structure. Again, the scattering parameters of the overall structure are easily obtained from this result, by applying equations (2.11_d) and (2.11_e).

A Matlab program was written to perform the described tasks for a structure consisting of N unit cell segments. The program scans over a specified frequency range and plots the magnitudes of the input reflection coefficient S_{11} and the transmission coefficient S_{21} on a decibel basis. These scattering parameters were discussed in section 2.2. Furthermore, the program generates another plot, showing the phase of the coefficient S_{21}, which represents the phase difference between the transmitted wave at the output and the

incident wave at the input of the microstrip structure with multilayer substrate. For the case with $N = 5$ segments, the S-parameters plots are shown in Fig. 3.6_a and Fig. 3.6_b.

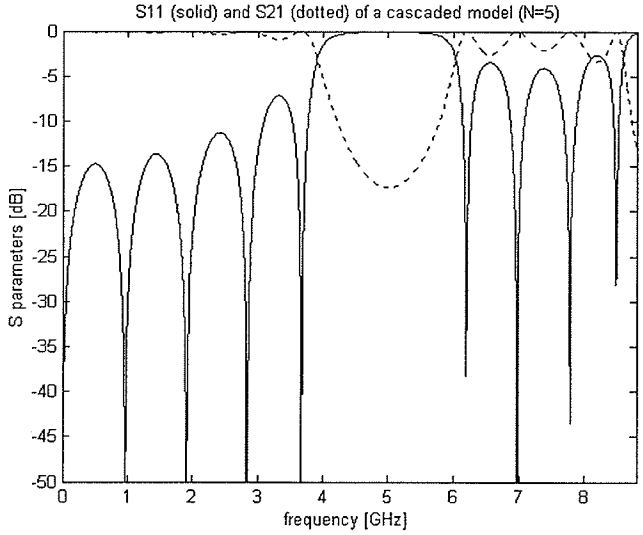

Fig. 3.6_a S- parameters for a cascaded line model with N=5 segments
($l_1 = 9mm, l_2 = 5mm, \varepsilon_{e1} = 7.21, \varepsilon_{e2} = 1, Z_{01} = 50\Omega, Z_{02} = 133.24\Omega$)

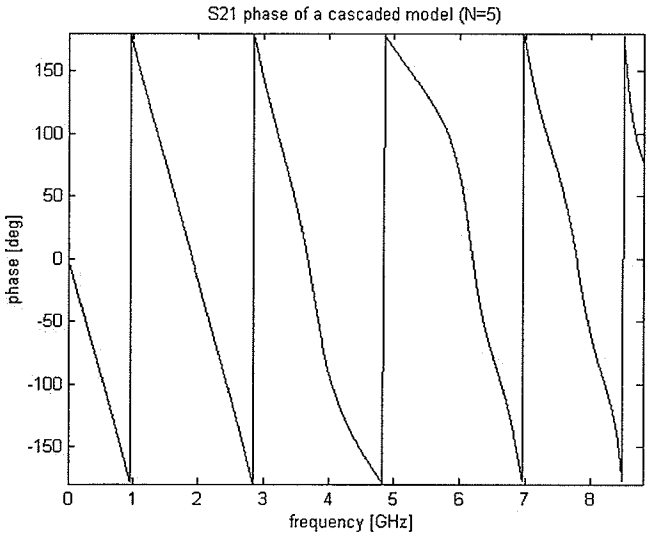

Fig. 3.6_b Phase diagram of a cascaded line model with N=5 segments
($l_1 = 9mm, l_2 = 5mm, \varepsilon_{e1} = 7.21, \varepsilon_{e2} = 1, Z_{01} = 50\Omega, Z_{02} = 133.24\Omega$)

For the case with N=15 segments, the two plots are given in the Fig. 3.7_a and Fig. 3.7_b, respectively.

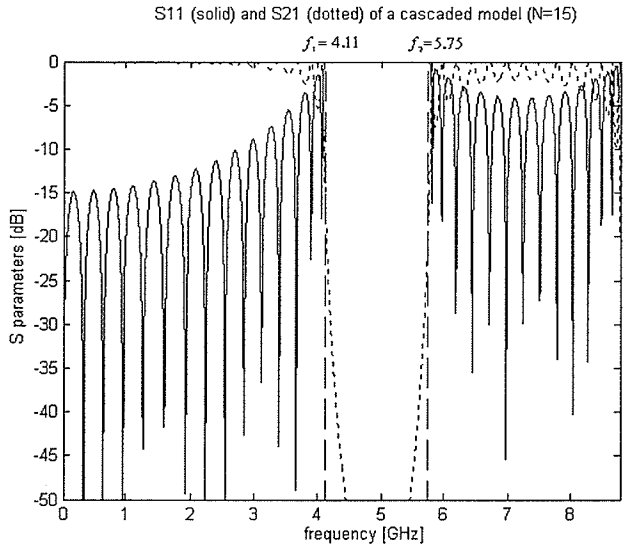

Fig. 3.7_a S- parameters for a cascaded line model with N=15 segments
$(l_1 = 9mm, l_2 = 5mm, \varepsilon_{e1} = 7.21, \varepsilon_{e2} = 1, Z_{01} = 50\Omega, Z_{02} = 133.24\Omega)$

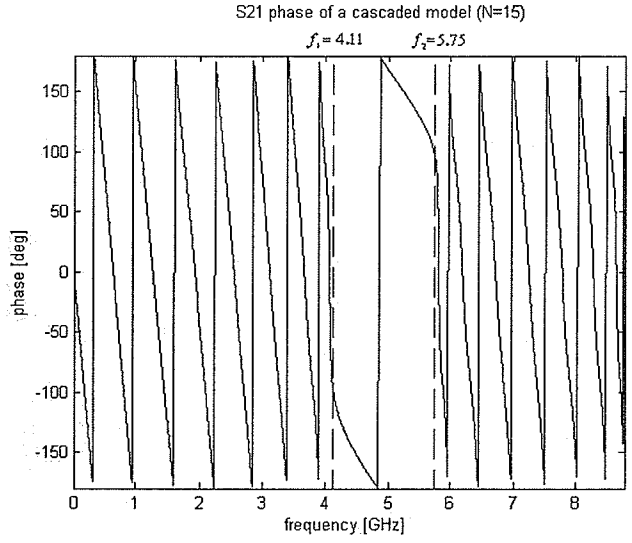

Fig. 3.7_b Phase diagram of a cascaded line model with N=15 segments
$(l_1 = 9mm, l_2 = 5mm, \varepsilon_{e1} = 7.21, \varepsilon_{e2} = 1, Z_{01} = 50\Omega, Z_{02} = 133.24\Omega)$

As discussed previously, for an infinite line structure we would expect the stopband to be perfectly defined between f_1=4.11 *GHz*, and f_2=5.75 *GHz*. As shown in the Fig. 3.6_a, already for 5 unit cell segments, the bandgap starts to be defined approximately within this frequency range. The input reflection coefficient S_{11} is close to 0 *dB*, while the transmission coefficient S_{21} is fairly small within the stopband, suggesting that almost the entire signal is reflected. Furthermore, the phase of the transmitted signal is fairly nonlinear within the stopband, suggesting the waveforms in the structure are very close to standing waves (Fig. 3.6_b). On the other hand, the transmitted signal phase within the passband is reasonably linear, especially at lower frequencies. As expected, the more pronounced bandgap effects are observed for *N*=15 unit cell segments, as shown in Fig. 3.7_a and Fig. 3.7_b. The stopband within this structure is practically the same as the one for theoretically infinite multilayer structure analyzed in the previous section. The input reflection coefficient at very low frequencies is smaller than –15 *dB*, which corresponds to structure's worst case input impedance of Z_{in}=72Ω, as per equation (2.6_b). Furthermore, if the equivalent homogeneous substrate with ε_e=4.34 is considered for low frequencies as given by (3.12), the worst input impedance mismatch will occur when the structure is quarter wavelength long, which yields the equivalent structure characteristic impedance of about Z_c=60Ω, as given by (2.6_a).

Finally, in order to qualitatively compare the band plots $\omega_n(k)$ of the structure under study and the plot from Fig. 2.16, a case with *N*=30 segments is considered. The phase

change within a unit cell is obtained by dividing the total structure phase with the number of segments N. The resulting band plot is shown in Fig. 3.8.

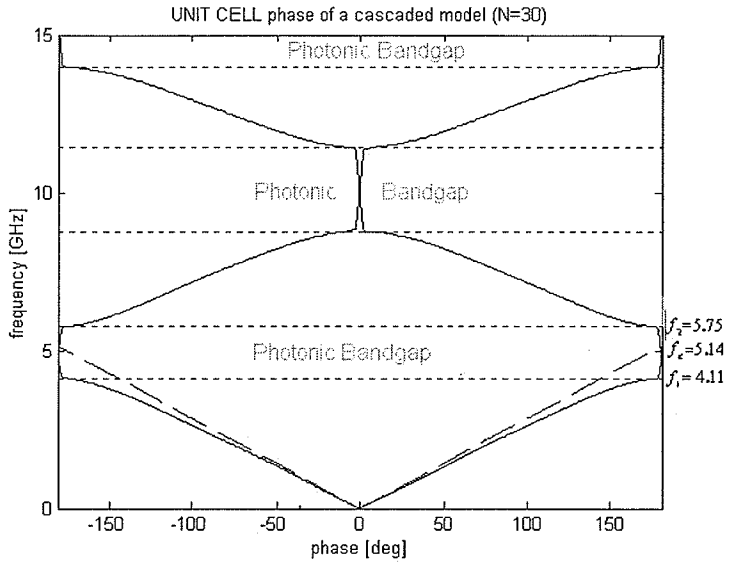

Fig. 3.8 The unit cell band plot of a cascaded line model with N=30 segments $(l_1 = 9mm, l_2 = 5mm, \varepsilon_{e1} = 7.21, \varepsilon_{e2} = 1, \boldsymbol{Z}_{01} = 50\Omega, \boldsymbol{Z}_{02} = 133.24\Omega)$

Only the first two band structures are shown in Fig. 3.8. The bandgap is sharply defined between the f_1=4.11 *GHz*, and f_2=5.75 *GHz*, as expected, while the next bandgap starts at approximately 8.75 *GHz*. The dashed straight lines represent the phase plot under the low frequency effective permittivity approximation, as given by (3.12). Under this assumption, the 180° phase change would occur at f_2=5.14*GHz*, as given by (3.13). The plot in Fig. 3.8 qualitatively agrees with the one of Fig. 2.16, while the quantitative agreement with the plot in Fig. 2.16 was obtained by choosing the corresponding cascaded line parameters in the equivalent circuit model.

Since a good agreement between the two models is observed, we can apply the PBG theory of an infinitely long multilayer film to a practically long transmission line with the multilayer substrate. However, the cascaded transmission line model seems to be simpler and gives the propagation information for frequencies outside of the stopband as well. That is the reason for considering the inverse application, where a multilayer photonic crystal discussed in the previous section is replaced by corresponding transmission line sections, which yield the same effective permittivity values. The microstrip line dimensions are then chosen in a way that the first region within the unit cell yields the characteristic impedance matched to the system impedance. The same dimensions are kept for the other layer, and its characteristic impedance is calculated. For a practically large number of segments, we can use this model to analyze the original problem of an infinitely long photonic crystal. The important prerequisite for the equivalence of these two models is the absence of any metallic discontinuities in a transmission line structure. The effects of metallic discontinuities will be studied in Chapter 5. The studied model relies on a one-dimensional microstrip line approximation and yields a high accuracy in solving the one-dimensional multilayer stack problem. However, in order to determine the model validity for an actual microstrip structure, a full wave simulator would need to be used. The models developed in Chapter 5 were verified with such a simulator, showing a good agreement.

3.3 Conclusion

In this chapter a numerical method is presented, which calculates the frequency bandgap intervals of a multilayer film structure. The method relied on the fact that the waves within the structure are standing waves at the bandgap edge frequencies. Furthermore, the symmetries in the wave patterns due to Bloch's theorem are made use of, as well as the electric and magnetic field continuity requirements at the dielectric interfaces. The method developed showed a perfect agreement with the more complicated methods reported in [2], which compute the entire band structure, not just the band edge frequencies, by using extensive minimization techniques.

Furthermore, the microstrip lines with multilayer dielectric substrates are presented. In one-dimensional approximation, it was shown that they could be modeled as multilayer films with the equivalent effective permittivity values, and the same dimensions. For these models to be equivalent, the microstrip line needs to have relatively large number of unit cell segments.

Finally, a microstrip structure with a multilayer substrate is modeled as a cascaded connection of transmission lines segments, and analyzed using the network theory presented section 2.2. A Matlab program was written to compute the scattering parameters of the structure, showing a good agreement with the photonic crystal model, for a large number of line segments. This approach will be used in Chapter 5 as well, where equivalent circuit is developed for a microstrip structure with metallic discontinuities in the ground plane.

Chapter 4

Microstrip Transmission Lines with Circular Ground Plane Perforations

This chapter covers the microstrip transmission lines with periodically etched circles in the ground plane and it is divided into two sections. The first section introduces the concept of PBG structures in the form of etched ground plane circles, along with a few examples published in literature. Furthermore, the measurement results obtained on several structures fabricated for this thesis are compared with the results simulated with Ansoft "Ensemble" full wave simulator. The second section presents the near-field scanning results for the fabricated structures, obtained with a probe connected to the Vector Network Analyzer (VNA).

4.1 Microstrip Lines with Circular Ground Plane Perforations

In the previous chapter it was mentioned that a frequency bandgap in microstrip lines is achievable by periodically contrasting the dielectric material in the substrate. The PBG effect is caused by multiple wave reflections, occurring at the periodic discontinuity interfaces. The similar effect can be produced by periodical discontinuities in the conducting surfaces of the structure, not just by its dielectric substrate discontinuities. A microstrip structure that has metallic discontinuities in the form of a single row of circles etched in the ground plane and aligned under the trace conductor is shown in Fig. 4.1.

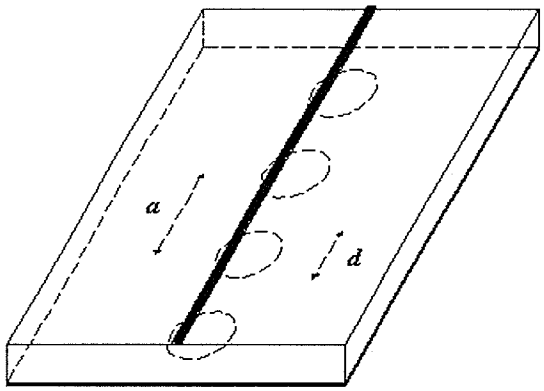

Fig. 4.1 Geometry of a microstrip line with circular ground plane perforations

A similar structure, having 3 rows of ground plane holes was previously investigated by Radisic and Qian [6]. However, due to high field concentration under the top conductor in a microstrip line structure, the design with only one row of ground plane perforations performs practically as well as the structure with 3 rows of holes. The etched ground plane structures analyzed and reported in [6] had the effective permittivity close to the permittivity of unperturbed structure with ground plane left intact. Therefore, the center stopband frequency approximately corresponds to the wavelength on the unperturbed microstrip structure that is twice the etched structure's period. Furthermore, the etched circles diameter is observed to be proportional to the stopband bandwidth. However, the only way to determine the center stopband frequency and the bandwidth of the structure is by a full wave simulation, as reported in [6]. Therefore, for a specific synthesis problem, a trial and error method needs to be used in order to meet the design

specification. This method is not very convenient, due to relatively long time required to solve, using full wave simulations.

In order to verify the results reported in [6] specific structures were designed, simulated and fabricated. The unperturbed microstrip line was fabricated on a substrate of thickness $h=0.635\ mm$ and relative permittivity $\varepsilon_r = 10.8$. The trace conductor width was $w=0.554\ mm$, corresponding to the characteristic impedance of $Z_c = 50\Omega$, as shown in Fig. 4.2_a. The fabricated line was $86mm$ long, while the effective dielectric constant is calculated to be $\varepsilon_e = 7.21$, yielding a wavelength of $\lambda = 28mm$ at the design frequency of $f = 4GHz$. This microstrip line structure was simulated with Ansoft "Ensemble" full wave simulator, and the 2-port scattering parameters are compared with the corresponding measured parameters, as shown in Fig. 4.2_b.

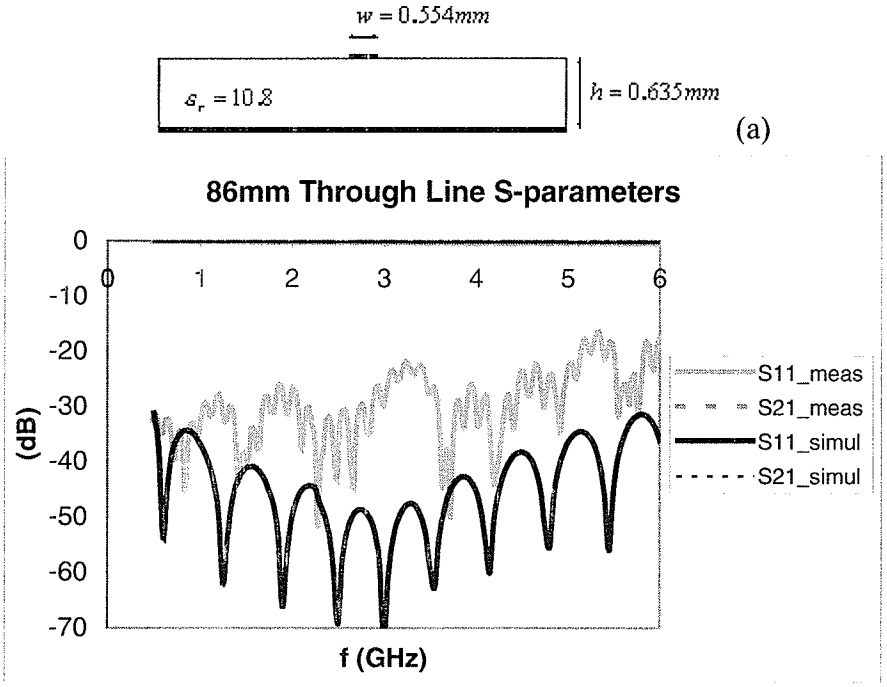

Fig. 4.2 Geometry (a) and measured and simulated scattering parameters (b) for an 86mm long unperturbed microstrip line

The black solid line represents "Ensemble" simulated input reflection coefficient S_{11} of the line, while the grey solid line represents the same coefficient obtained by VNA measurements performed on the fabricated structure. The idealized simulated structure has the input reflection coefficient lower than –30 *dB*, while the measured parameter is lower then –18 *dB*. According to (2.6), these values correspond to the deviation from the system impedance of $50\pm1.6\Omega$ for the simulated and $50\pm6.7\Omega$ for the fabricated structure. The simulated and measured insertion loss S_{21} is $-0.3dB$ and $-0.65dB$, respectively. The measured characteristic has a noisy ripple due to the calibration errors, since the end effects of the test fixture used to connect the structure to the VNA are not included. Furthermore, due to the milling errors, the structure characteristic impedance deviates from the system impedance, causing the larger ripple in the S_{11} pattern. The measured and simulated phase plots along the unperturbed line are shown in Fig. 4.3.

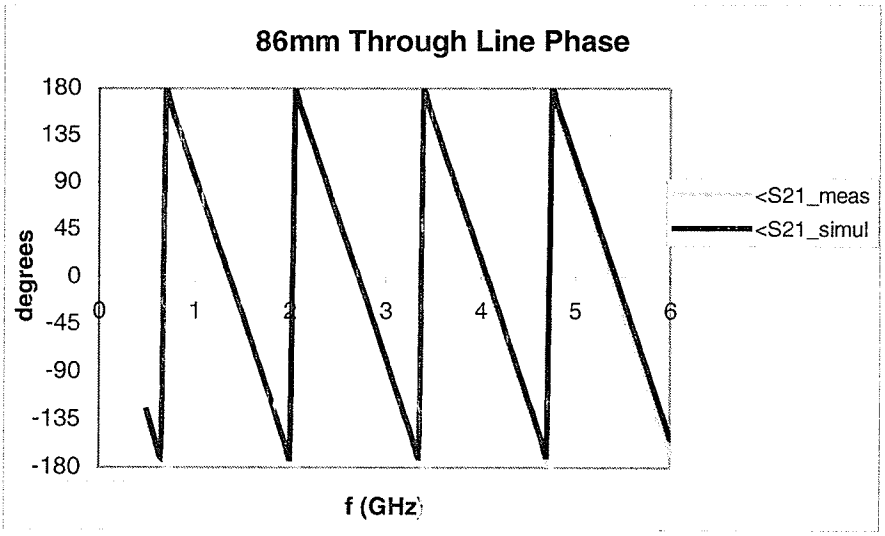

Fig. 4.3 Measured and simulated phase for an 86mm long unperturbed microstrip line

The measured phase change represented by grey line originally had a smaller slope, suggesting smaller effective permittivity than previously predicted, namely $\varepsilon_e = 7.21$. A reliable method presented in section 4.2 estimated the effective permittivity of the fabricated structure to be $\varepsilon_e = 6.83$, at the design frequency of $4GHz$. This result is taken into account by reducing the substrate dielectric constant of the simulated structure from $\varepsilon_r = 10.8$ down to $\varepsilon_r = 10.3$, which now yields $\varepsilon_e = 6.83$. The revised dielectric constant value is used for obtaining all simulation results in this chapter, including the ones shown in Fig. 4.2 and Fig. 4.3. The effective permittivity can also be estimated from the phase characteristic, by using the expression (2.3). Since the phase characteristic slope changes with frequency, one can determine the effective permittivity values by averaging the slope in the frequency ranges of interest. Table 4.1 contains the effective permittivity values for the fabricated structure, obtained by the slope averaging method.

Table 4.1. Transmission line effective permittivity values obtained from the measured S_{21} phase

f_{ave} (GHz)	f_1 (GHz)	f_2 (GHz)	Δf (GHz)	$\Delta\theta$ (°)	ε_e
1.35	0.69	2.01	1.32	349.91	6.598
2.70	2.04	3.36	1.32	352.45	6.694
4.05	3.39	4.71	1.32	354.80	6.784
5.37	4.74	6.00	1.26	343.49	6.978

The frequencies f_{ave} at which the effective permittivity is estimated are given in the first column of the table. These values are the mean values of individual near-linear segments of the phase characteristic from Fig. 4.3. From the last column in Table 4.1, we notice

that the effective permittivity of the fabricated structure slightly increases with frequency, due to the increase in the field concentration underneath the trace conductor. The ε_e value around the design frequency of $4GHz$ obtained from Table 4.1 (i.e. $\varepsilon_e = 6.784$), is relatively close to the value obtained in section 4.2, namely $\varepsilon_e = 6.83$.

The losses due to radiation, surface waves, conductor and dielectric loss are obtained by subtracting transmitted and reflected power from the incident wave power (i.e. $1-|S_{11}|^2-|S_{21}|^2$), and they are shown in Fig. 4.4.

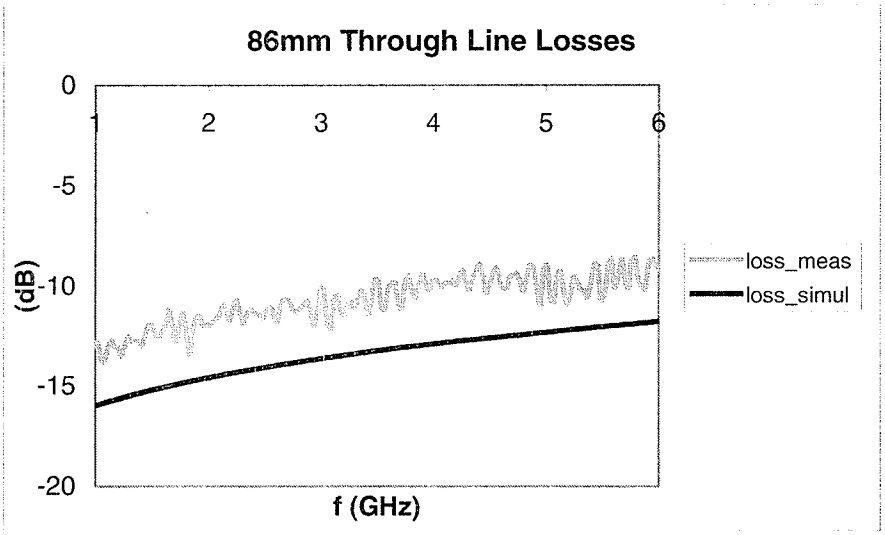

Fig. 4.4 Measured and simulated losses for an 86mm long unperturbed microstrip line

The dimensions of the design microstrip line, substituted into expressions (2.24-2.26), yield the critical frequencies of f_1=50.2GHz, f_2=6.11GHz, f_3=56.5GHz. Since all these values are outside of the frequency range of interest (f<6GHz), the losses due to radiation and surface waves are relatively small, implying that overall losses shown in Fig. 4.4, which are less than $-10dB$, mostly consist of conductor and dielectric losses.

The next structure under investigation is a microstrip structure having the same dimensions, with the addition of circular holes etched in the ground plane. A single row of 5 holes with diameters of $d = 5mm$ each are spaced at $a = 14mm$, which is approximately half the wavelength of the unperturbed structure, at the design frequency of $f = 4GHz$. The line is $86mm$ long, which is $16mm$ longer than the length of 5 unit cells, ($5a$=$70mm$). The spare length of $8mm$ unperturbed line on each side is added, in order to reduce coupling with the test fixture walls. The measured scattering parameters of the fabricated structure are compared with the corresponding parameters obtained by the "Ensemble" simulation, as shown in Fig. 4.5.

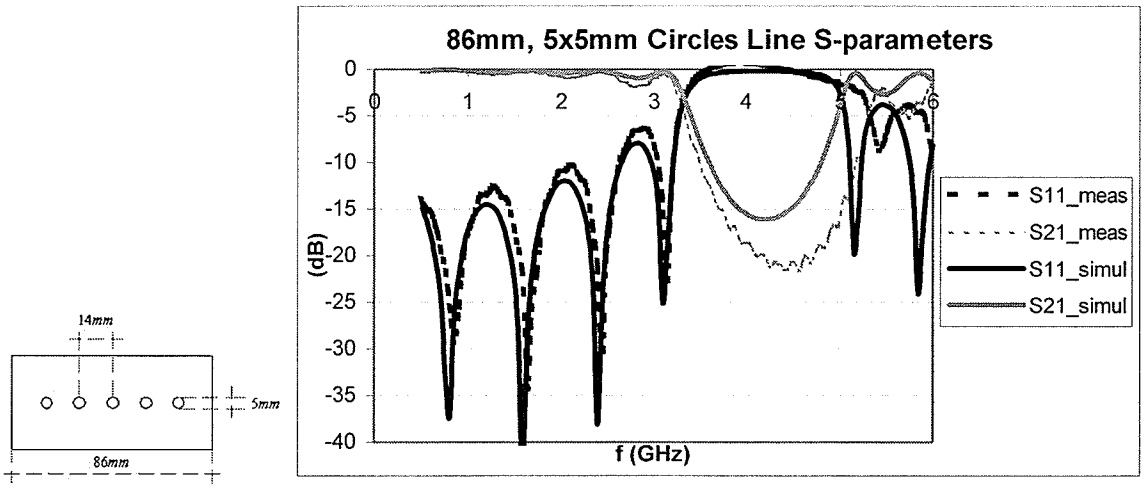

Fig. 4.5 Measured and simulated S- parameters for an 86mm long microstrip line with 5 ground plane etched circles of d=5mm, spaced at a=14mm

The insertion loss S_{21} at the design center stopband frequency $f = 4GHz$ is -16dB for simulated structure, and –18dB for the fabricated one. At the design frequency, the return loss S_{11} of the simulated and fabricated structure is –0.2dB and –0.6dB, respectively. The simulated and measured parameters are in a relatively good agreement, given that the test

fixture effects are not accounted for. Furthermore, the phase shift $\angle S_{21}$ of the simulated structure is compared to the measured one, as shown in Fig. 4.6.

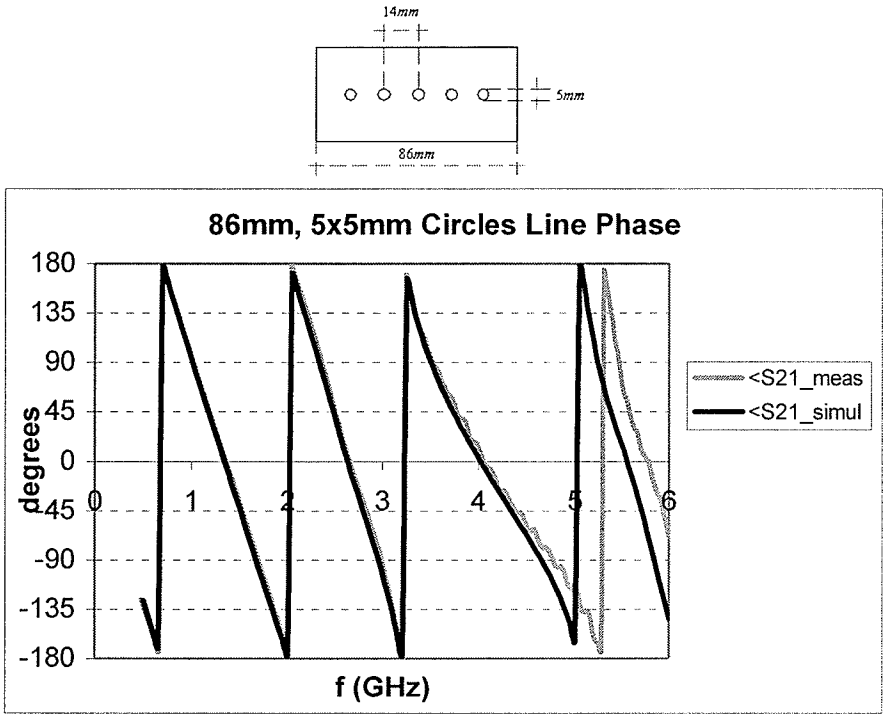

Fig. 4.6 Measured and simulated phase for an 86mm long microstrip line with 5 ground plane etched circles of d=5mm, spaced at a=14mm

As expected, the ground plane perforations caused a frequency stopband, approximately centered at 4 *GHz*, as shown in Fig. 4.5. The filter bandwidth for simulated structure is defined at -3*dB* points of the transmission coefficient $\boldsymbol{S}_{21}$, which happens to be between $f_{lo} = 3.25GHz$ and $f_{hi} = 4.95GHz$. The corresponding mean stopband frequency is $f_c = 4.1GHz$, which is slightly higher than the initial design frequency of $f_d = 4GHz$. The increase in the center frequency is due to the smaller effective permittivity of the etched ground plane structure, where larger portion of the field lines are linked through

the air, as compared to the unperturbed structure. Furthermore, as discussed in Chapter 3, even for the infinite multilayer PBG structure, the mean bandgap frequency does not necessarily coincide with the frequency corresponding to the structure's effective permittivity approximation at low frequencies. The effective permittivity of the simulated structure is estimated from Fig. 4.6 at specific frequencies, and shown in table 4.2.

Table 4.2. Perforated transmission line effective permittivity values obtained from simulated S_{21} phase, for the structure with 5 holes having d=5mm and a=14mm

f_{ave} (GHz)	f_1 (GHz)	f_2 (GHz)	Δf (GHz)	$\Delta\theta$ (°)	ε_e
1.35	0.70	2.00	1.30	354.16	7.134
2.63	2.05	3.20	1.15	345.21	8.661
3.70	3.40	4.00	0.60	109.53	3.203
5.53	5.05	6.00	0.95	320.92	10.97

The transmission coefficient phase is highly nonlinear inside the frequency stopband region, suggesting a significant presence of standing waves, as expected. Consequently, the effective permittivity value is estimated at a frequency closer to the stopband lower edge, namely $3.70GHz$, rather than at the center bandgap frequency. As intuitively expected, the effective permittivity within the stopband region is smaller than the permittivity of the unperturbed structure. However, the passband effective permittivity of the etched holes structure is higher than the one of the unperturbed structure. This somewhat surprising observation is caused by the metallic discontinuities in the ground plane, which affect the signal phase, even at low frequencies.

In order to demonstrate the effect of the etched holes diameter on the filter bandwidth, another structure is designed and fabricated. The periodic spacing between the 5 holes

remains $a = 14mm$, while the holes diameter is increased to $d = 10mm$. Again, the measured scattering parameters of the fabricated structure are compared with the corresponding simulation parameters in Fig. 4.7, while the corresponding phase characteristics are shown in Fig. 4.8. The insertion loss S_{21} at the design center stopband frequency $f = 4GHz$ has decreased to -40dB for simulated structure, and –35dB for the fabricated one.

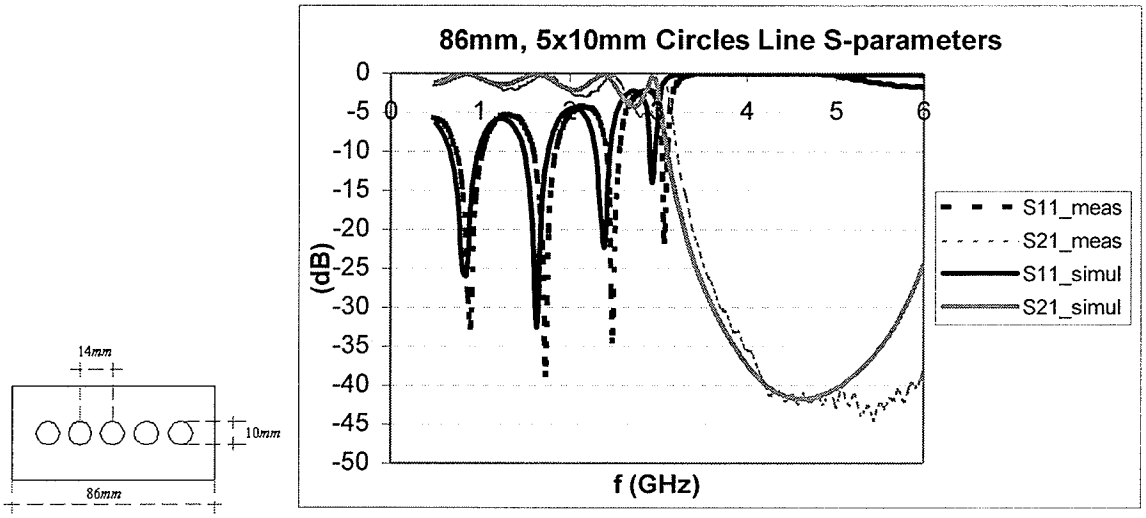

Fig. 4.7 Measured and simulated S- parameters for an 86mm long microstrip line with 5 ground plane etched circles of d=10mm, spaced at a=14mm

The filter bandwidth for simulated structure defined at -3dB points of transmission coefficient S_{21} falls between $f_{lo} = 2.95GHz$ and $f_{hi} = 6.05GHz$. As expected, the bandwidth has increased considerably, as well as the mean stopband frequency, which is now $f_c = 4.5GHz$. The structure effective permittivity within the stopband region is further decreased, as compared with the smaller holes diameter structure. Similarly, the effective permittivity within the passband region is further increased. The reflection

coefficient within the passband is also increased for larger holes diameter, causing a tradeoff between the filter bandwidth and the passband insertion loss.

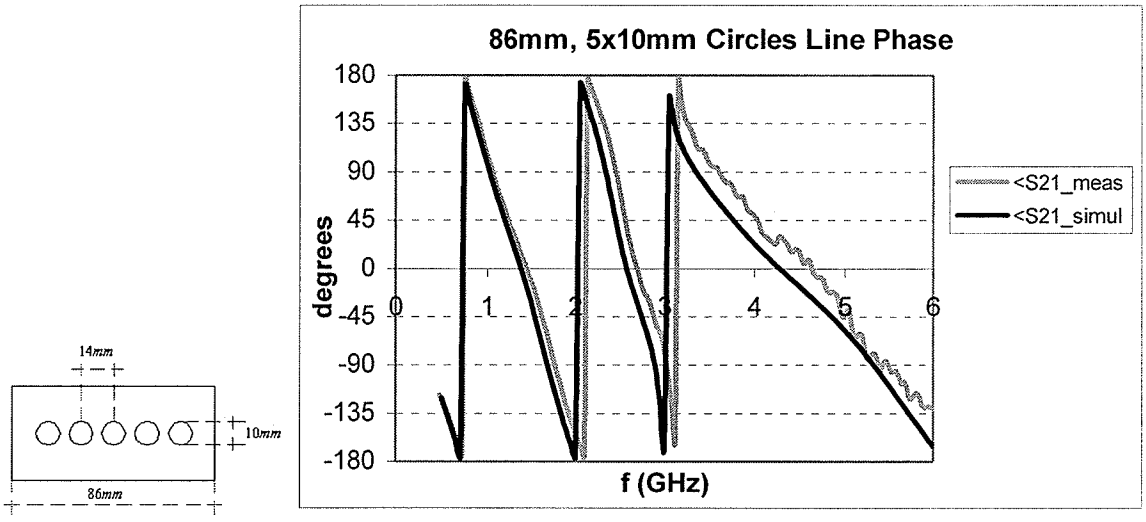

Fig. 4.8 Measured and simulated phase for an 86mm long microstrip line with 5 ground plane etched circles of d=10mm, spaced at a=14mm

In summary of this section, the PBG microstrip structures with etched ground plane holes are investigated. The stopband center frequency and the bandwidth are related to the period and the diameter of the holes, respectively. However, their exact values need to be determined by a full wave electromagnetic simulator, such as "Ensemble" used here. The coupled mode theory was also successfully applied to analysis of these structures, as reported in [7]. The basic idea of this method is that the fields at any cross section of a nonuniform waveguide can be represented as a superposition of the different modes corresponding to a uniform auxiliary waveguide with the same cross section and the identical distribution of dielectric permittivity and magnetic permeability. Finally, the measurement results on the two fabricated PBG structures confirmed the direct

relationship between the stopband bandwidth and the diameters of the etched holes. A good agreement with the full wave simulated results was obtained.

4.2 Near-Field Scans of Circular PBG Microstrip Structures

In order to get an insight into the fields distribution of the investigated structure, an electrical scanning probe system is assembled at the lab, as illustrated in Fig. 4.9.

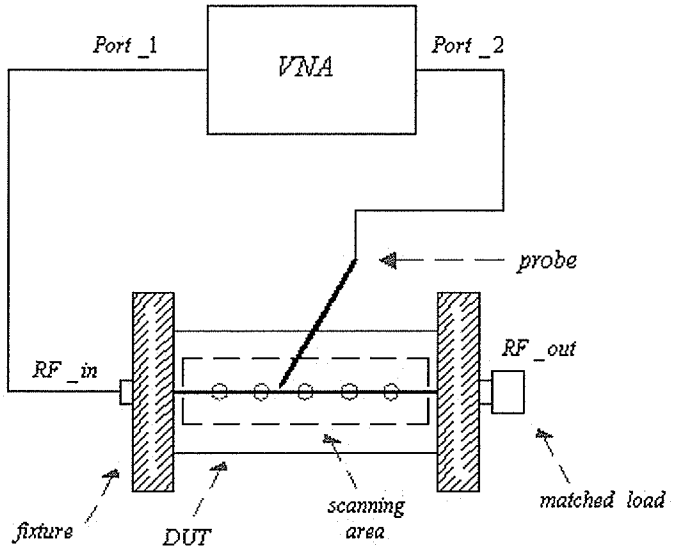

Fig. 4.9 Near-field scanning assembly

The fabricated PBG microstrip structures (i.e. device under test – DUT) were fitted into a text fixture and connected to the Vector Network Analyzer (VNA). The microstrip line is excited at one end with a single frequency signal from VNA, and match terminated at the other end. The probe connected to the second port of the VNA is normal to the top surface, and it is kept at small height above it. As the probe is moved above the scanning area illustrated in Fig. 4.9, it captures the vertical component of the electric near-fields, as

shown in Fig. 4.10. This information will reveal the points where the electric fields become horizontal at the probe height, as well as give a general idea about the strength of overall electric fields, which are illustrated in Fig. 2.7.

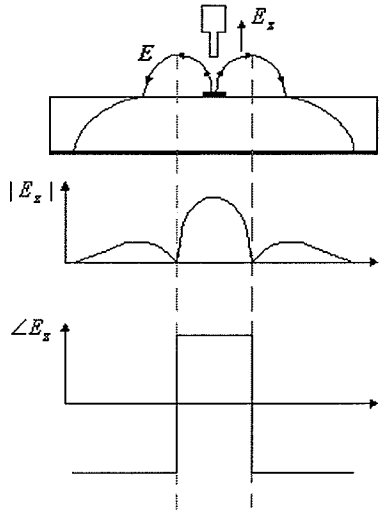

Fig. 4.10 Near-field lateral scanning illustration

The vertical component of the electric field E_z magnitude scan results for the 86*mm* long unperturbed microstrip structure are shown in Fig. 4.11, at excitation frequency of $f = 4GHz$.

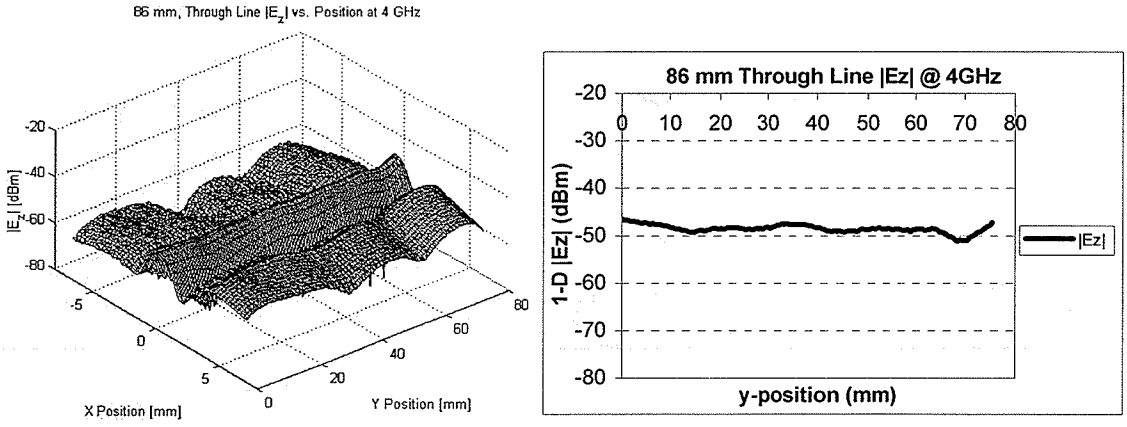

Fig. 4.11 Ez magnitude scan for an 86mm long match terminated microstrip line at f=4 GHz, 2-D (left) and 1-D (right)

The scanned E_z phase results for the same structure and frequency are shown in Fig. 4.12.

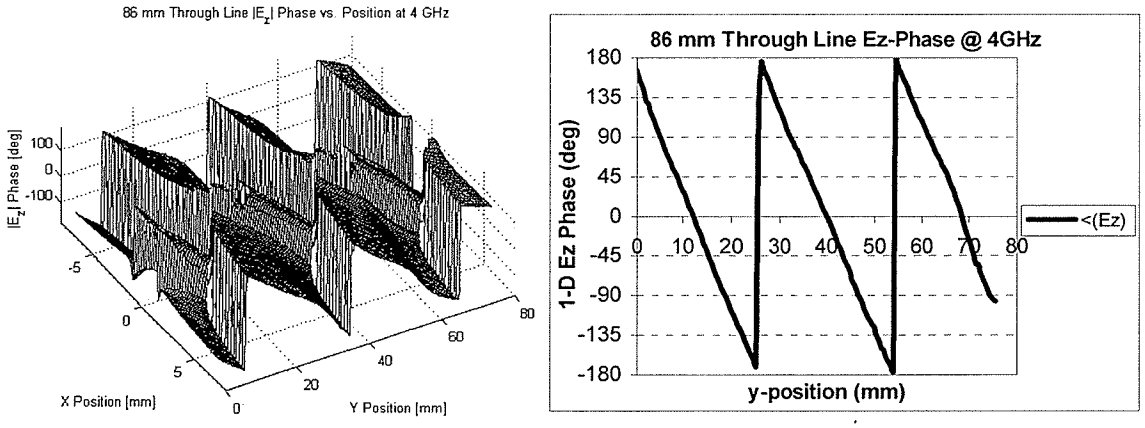

Fig. 4.12 Ez phase scan for an 86mm long match terminated microstrip line at f=4 GHz, 2-D (left) and 1-D (right)

The microstrip line axis is positioned along y-direction, and the trace conductor is centered at x=0 position. As expected, the probe signal is the strongest along the trace center and it does not get higher than –45 *dBm*, since the probe is non-contacting. A very small ripple in the relative voltage magnitude along the trace conductor suggests a good match of the line characteristic impedance Z_c to the system impedance of 50Ω. The difference in signal level at the line ends is –0.8*dB*, which is close to –0.6*dB* insertion loss, estimated in section 4.1. The electric fields are getting more horizontal away from the center conductor, as shown in Fig. 2.7. Since the voltage magnitude shown in Fig. 4.10 captures only the vertical component E_z of the electric fields, the shown voltage magnitude drops at a high rate away from the trace conductor. Furthermore, the total electric fields are concentrated mostly around the trace, resulting in an even faster drop of the voltage shown in Figure 4.10. The direction of E_z changes at the points where total

electric fields are horizontal, as illustrated in Fig. 2.7. The abrupt change in E_z phase appears as a shift in the center wave front, as shown in 2-dimensional plot of Fig. 4.12. The plane wave fronts are clearly visible in the Figure, indicating the quasi-TEM mode of operation. Furthermore, the phase plot is fairly linear, indicating a negligible signal reflection. Finally, the effective signal wavelength of λ_e=28.7*mm* was estimated from the one-dimensional plot in Fig. 4.12, as the distance for which the phase undergoes a change of 360°. This value corresponds to the effective permittivity of ε_e=6.83, according to expression (2.3), which is close to the frequency sweep VNA result obtained in section 4.1, namely ε_e=6.78.

The next microstrip structure under study is similar to PBG structure in Fig. 4.1, except that it has a single row of 5 holes with diameters of $d = 5mm$ each, spaced at $a = 14mm$. The vertical component of the electric field E_z magnitude scan results for this structure is shown in Fig. 4.13, while its phase is shown in Fig. 4.14, both at f=1.68*GHz*, which is in the passband.

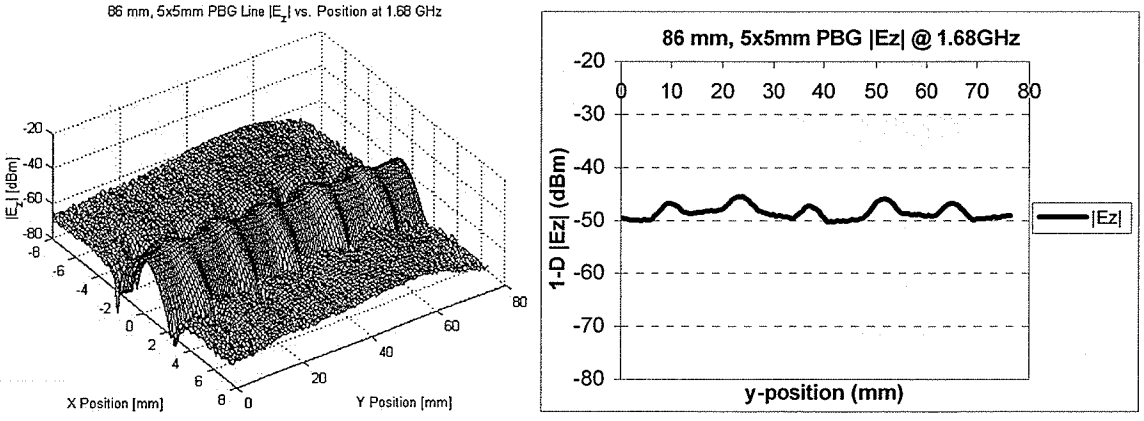

Fig. 4.13 Ez magnitude scan at f=1.68GHz for an 86mm long microstrip line with 5 ground plane etched circles of d=5mm, spaced at a=14mm, 2-D (left) and 1-D (right)

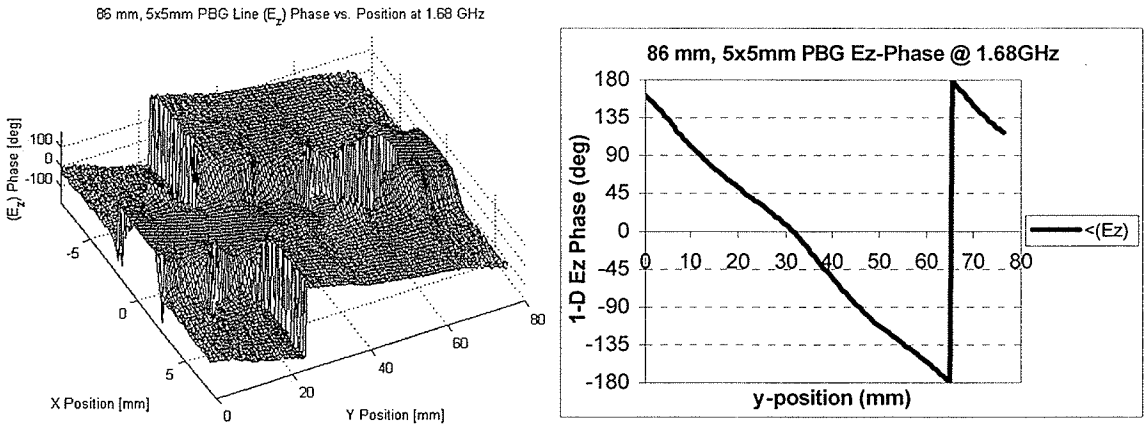

Fig. 4.14 Ez phase scan at f=1.68GHz for an 86mm long microstrip line with 5 ground plane etched circles of d=5mm, spaced at a=14mm, 2-D (left) and 1-D (right)

The presence of holes is visible as a small ripple in Fig. 4.13, and the insertion loss of the line is about $-0.5dB$. The effective signal wavelength of λ_e=$67mm$ was estimated from the one-dimensional plot in Fig. 4.14. This value corresponds to the effective permittivity of ε_e=7.11 at the given frequency, which is close to the value estimated in section 4.1, namely ε_e=7.13. The signal level further away from the trace conductor is also increased, as compared with the unperturbed structure. This effect is due to the etched ground plane holes, since the electric field lines are forced to close on the ground conductor around the circles.

The near-field E_z magnitude scans for the same structure were performed at the design stopband frequency of $4GHz$, and shown in Fig. 4.15. The transmitted signal decays along the line, as evident from Fig. 4.15. The insertion loss is about $-20dB$, which agrees

with the observation from Fig. 4.5, at $4GHz$. The scan results for E_z phase are shown in Fig. 4.16.

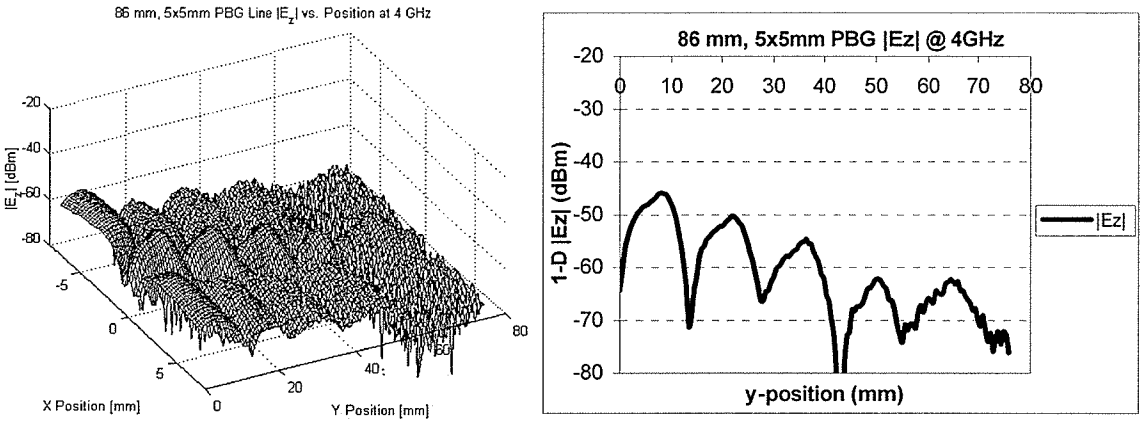

Fig. 4.15 Ez magnitude scan at f=4GHz for an 86mm long microstrip line with 5 ground plane etched circles of d=5mm, spaced at a=14mm, 2-D (left) and 1-D (right)

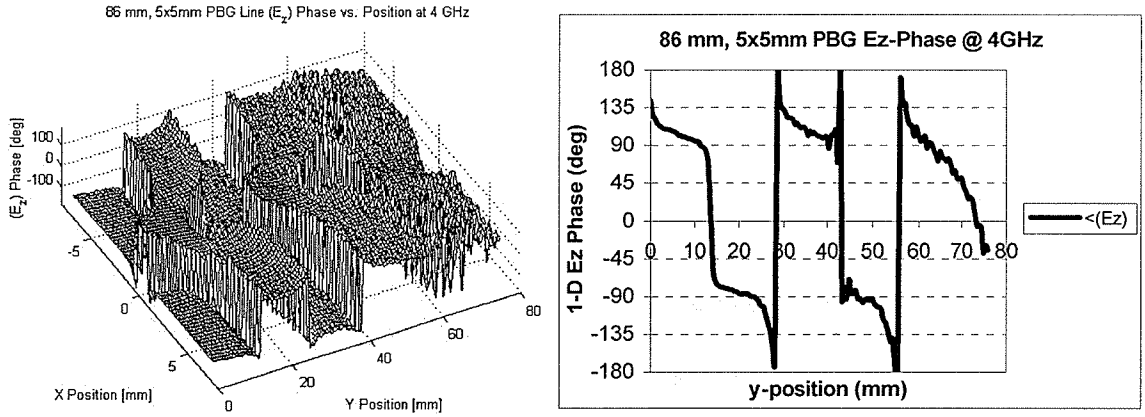

Fig. 4.16 Ez phase scan at f=4GHz for an 86mm long microstrip line with 5 ground plane etched circles of d=5mm, spaced at a=14mm, 2-D (left) and 1-D (right)

In order to get a better insight into the field configuration around etched holes, a 30 *mm* long microstrip structure is fabricated, with a single hole of diameter $d = 10mm$. The

near-field E_z magnitude scans for this structure were performed at the design stopband frequency of $4GHz$, and shown in Fig. 4.17.

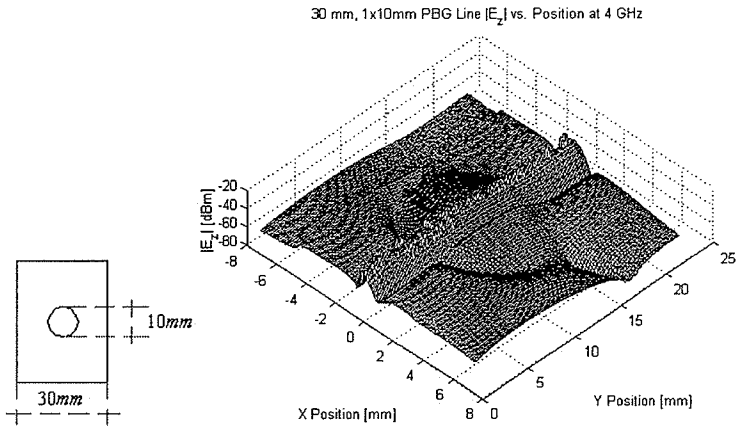

Fig. 4.17 Ez magnitude scan at f=4 GHz for a 30mm long microstrip line with 1 ground plane etched circle of d=10mm

The etched circle pattern is clearly visible, confirming the fact that electric field lines extend further away from the trace conductor, as compared with the unperturbed structure.

4.3 Conclusion

In this chapter microstrip transmission lines with circular ground plane perforations were studied. It was shown that periodically etched holes in the ground plane caused a frequency stopband in the structures response characteristics. The effects of hole dimensions and period on the structure performance were studied in detail. It was concluded that the center stopband frequency is inversely proportional to the circle period, while the filter bandwidth is directly proportional to the circle diameter. The effective permittivity was obtained from the transmission coefficient phase characteristic.

It was concluded that the etched ground holes cause the increase in the effective permittivity in the passband region, while the permittivity is decreased within the stopband region. Finally, near-field probe scans at discrete frequencies provided more insight into the field configurations within these structures. It was concluded that by etching the holes in the ground plane, the electric fields are spread further away from the top trace conductor, in order to close at the ground plane circle perimeters. The one-dimensional near-field scans at discrete frequencies along the axis of the line, confirmed the results obtained from port frequency sweep measurements.

Chapter 5

Microstrip Transmission Lines with Rectangular Ground Plane Perforations

This chapter covers the microstrip transmission lines with periodically etched rectangles in the ground plane. The chapter is divided into 2 sections, where the first one covers the numerical methods for estimating the characteristic impedance and the effective permittivity of an individual microstrip line section with an etched rectangular strip along the entire ground plane. In the second section, an equivalent circuit model is developed for the entire structure with periodical rectangular perforations.

5.1 Microstrip Lines with a Split Ground Plane

In the previous chapter it was mentioned that a frequency bandgap in microstrip lines is achievable by periodic discontinuities in the metallic conductors, not just by discontinuities in the dielectric substrate. However, due to higher-order modes that metallic discontinuities produce, the equivalent circuit for these structures needs to be more complex than cascaded connection of transmission lines, used in Chapter 3. The structure presented in the previous chapter has one row of circular ground perforations. The original purpose of circular periodic PBG structures is to provide a rotational symmetry in 2 dimensions, as discussed in the background chapter. However, the dominant mode in a microstrip line propagates in one direction only, and the fields are concentrated mostly in the regions around the strip conductor. That is why a single row of

holes in the ground plane was performing almost the same as a two-dimensional lattice of perforations. Therefore, there is no need for having a rotational symmetry in the PBG microstrip line structures. Similar PBG effects are observed with square ground plane perforations, where the square dimensions relate to the stopband bandwidth. However, in order to obtain the network properties of these structures, a full wave simulator needs to be used. In this chapter, ground plane perforations in rectangular form are proposed, since they seem to be suitable for equivalent circuit modeling. The width of the rectangles is kept constant, while its length can be changed in the design to account for the desired stopband bandwidth. Therefore, the cross section of a microstrip line segment containing the rectangular perforation is uniform, and can be modeled as a transmission line with certain characteristic impedance and effective permittivity. The geometry of a microstrip line with rectangular ground plane perforations is illustrated in Fig. 5.1.

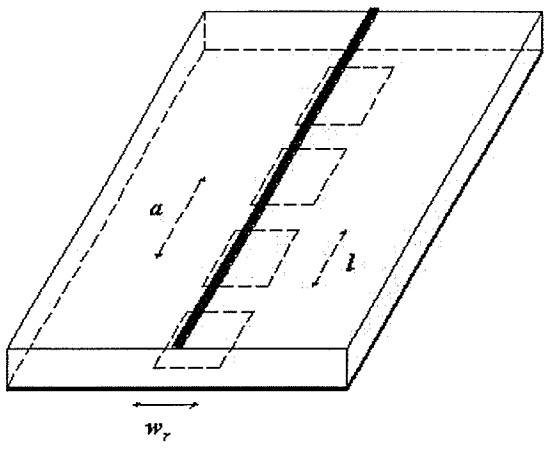

Fig. 5.1 Geometry of a microstrip line with rectangular ground plane perforations

A segment of the structure in Fig. 5.1 that contains a ground plane rectangle has a uniform cross section. Observed individually, such a segment appears as a microstrip line with the ground plane split into two parts. A cross sectional geometry of this structure is shown in Fig. 5.2 (right).

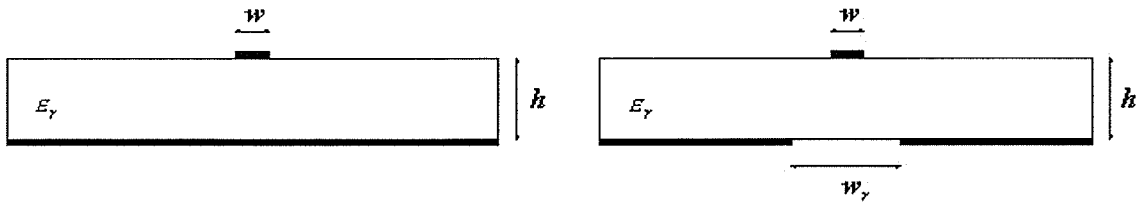

Fig. 5.2 Cross sectional geometry of a microstrip line with a ground plane gap (right) and a regular microstrip line (left)

The structure consists of a strip conductor of the width w, sitting on a substrate of height h, and dielectric constant ε_r, while the gap in the ground plane is of width w_r. For this geometry, no empirical expressions for the characteristic impedance or the effective permittivity are found in literature. Therefore, these parameters need to be obtained numerically. As discussed in section 2.3, one way to obtain these parameters for any geometry is by numerically solving the electrostatic Laplace equation (2.17). The boundary conditions for this equation require the constant voltage between the strip conductor and the ground plane, while the theoretically infinite cross section needs to be reasonably truncated and specified in terms of boundary conditions, as shown in Fig. 5.3. In this particular problem, the Neumann boundary conditions are chosen at the truncated boundary, stating that there are no voltage components normal to the boundary [3]. Once the Laplace equation is solved, the potential in the cross sectional region is known.

Therefore, the electric fields in the cross section can be determined by simply taking the gradient of the voltage as a 2-dimensional function of position.

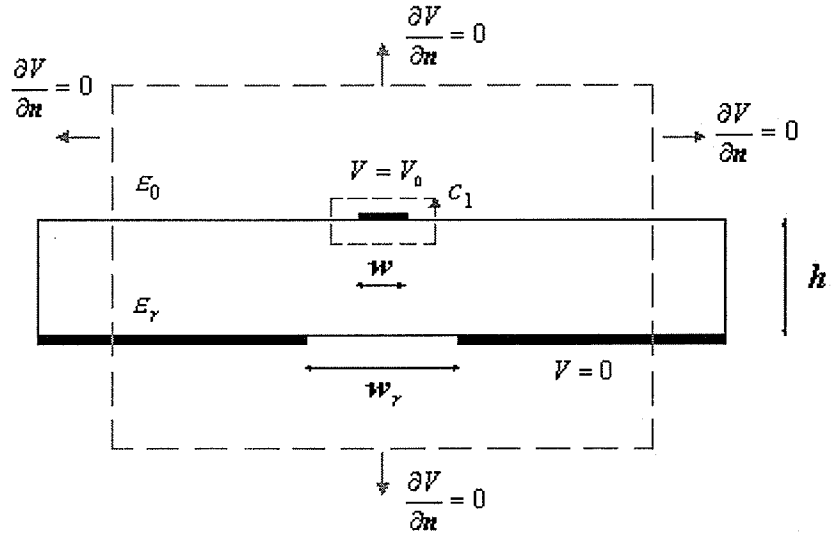

Fig. 5.3 Boundary conditions for numerical solution of a Laplace equation for a microstrip line with a ground plane gap

Finally, if a closed line is placed around the strip conductor, the total electric flux leaving this line will equal the total electric charge per unit length of the structure, according to Gauss's Law. In this case, the closed line around the conductor actually represents a cross section of a Gauss's surface with the unit length. The corresponding capacitance per unit length C is simply the ratio of the charge per unit length and the applied electrostatic voltage:

$$C\ [F/m] = \frac{Q\ [C/m]}{V_0} = \frac{\oint_{c_1} \varepsilon_0 \varepsilon_r \boldsymbol{E} d\boldsymbol{l}}{V_0} \qquad (5.1)$$

where c_1 is a line which encloses the strip conductor cross section, as shown in Fig. 5.3.

The inductance per unit length L of the structure is needed as well, in order to determine its characteristic impedance and the effective permittivity, as per formulas (2.4) and (2.3) respectively. The direct computation of L can be avoided for the structures with nonmagnetic substrates. The original structure in Fig. 5.2 will have the same inductance as the structure where the dielectric substrate is replaced by air, since the original dielectric is assumed to be nonmagnetic. Now the numerical method for solving the Laplace equation can be applied again, and consequently the capacitance per unit length of the modified structure C_{air} can be found. Finally, since this structure is completely surrounded by air, the speed of propagation will be the speed of light in free space, as given by:

$$\frac{1}{\sqrt{LC_{air}}} = c \qquad (5.2)$$

Consequently, the inductance per unit length L can be found from (5.2), and it is the same as L of the original structure. Once the L and C are known for a structure, one can find the characteristic impedance and the effective permittivity by:

$$Z_c = \sqrt{\frac{L}{C}} = \sqrt{\frac{1}{c^2 C_{air} C}} = \frac{1}{c\sqrt{C_{air} C}} \qquad (5.3\_a)$$

$$\varepsilon_e = c^2 LC = c^2 \frac{1}{c^2 C_{air}} C = \frac{C}{C_{air}} \qquad (5.3\_b)$$

Clearly form these equations, one can find Z_c and ε_e by finding the capacitance per unit length C of the original structure, and the capacitance per unit length C_{air} of an air filled structures with the same dimensions.

A Matlab program was written to perform the procedure described above. The Laplace equation is approximated by a difference formula, and the successive over-relaxation method is used to obtain the potential in the cross sectional region [3]. The demonstration example is obtain by removing a w_r=5*mm* strip in the ground plane, of a microstrip line with the top conductor width w=0.554 *mm*, sitting on a substrate of height h=0.635 *mm* and dielectric constant ε_r=10.8. For the structure with the same dimensions and ground plane left intact (w_r=0), the Matlab program estimated a characteristic impedance of Z_c=57.5 Ω, and the effective permittivity of ε_e=6.7. The truncated boundary used in simulation was 40*mm* wide and 20*mm* high, with a grid of 125x125 points used in the finite difference formula. The empirical formulas (2.22) and (2.21) yield Z_c=50 Ω and ε_e=7.21 for the same structure. Therefore, we can conclude that the error introduced by the Matlab program was within 8% for both parameters.

After the ground plane gap is introduced, one can expect a decrease in the capacitance per unit length, and therefore an increase in the characteristic impedance of the structure. Furthermore, a decrease in the effective permittivity is expected, since the air region takes a larger fraction of the dielectric medium than before, due to the presence of the electric fields in the air below the ground plane. The described Matlab program also plots

the equipotential lines for the cross section of the structure. For the mentioned example, these lines are shown in Fig. 5.4.

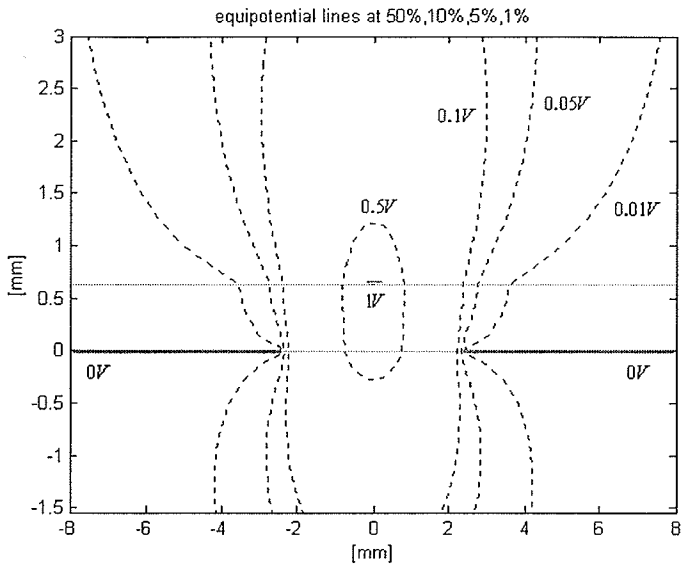

Fig. 5.4 Equipotential lines in a microstrip line with ε_r *=10.8, h=0.635 mm w=0.554 mm, and the ground plane gap* w_r *=5 mm*

The electric fields can be visualized as lines being orthogonal to the equipotential lines, starting at the top conductor, and sinking at the ground planes. Clearly, some of the electric filed lines are concentrated in the air region below the ground plane level ($y < 0$). In order to obtain C_{air}, the same program is run for a modified structure, when the dielectric substrate is replaced by air. The capacitances obtained were $C = 6.22 \times 10^{-11} F/m$ and $C_{air} = 1.65 \times 10^{-11} F/m$, respectively. Based on formulas (5.3_a) and (5.3_b), the characteristic impedance and the effective permittivity of the structure are estimated at Z_c=104.08 Ω and ε_e=3.77, respectively. As expected, the first

parameter has increased, while the second one has decreased, compared to the corresponding microstrip line structure with the ground plane left intact.

Since the Matlab program used resulted in a discrepancy of about 8% for the known structure parameters, the values obtained for the split ground plane structure (Z_c=104.08 Ω and ε_e=3.77) will be used only as initial values in section 5.2, and further optimized. The optimized values will be used in the equivalent circuit model for the entire structure with periodically etched rectangles.

5.2 Microstrip Lines with Rectangular Ground Plane Perforations

Having estimated the characteristic impedance and the effective permittivity of the line sections with an etched rectangle in the ground plane (Fig. 5.1), the next step is to model the transitions at the edges of these sections. The line sections adjacent to the etched rectangles can be thought of regular, unperturbed microstrip line segments, with the effective permittivity and the characteristic impedance given by (2.21) and (2.22), respectively. However, the metallic discontinuities in the ground plane will cause higher-order modes to be generated at the transitions, as discussed in section 2.3. The step in a microstrip line top conductor can be modeled with a T-junction of lumped elements, as shown in Fig. 2.10. The similar effect can be expected at the rectangular ground plane discontinuities, for the structure in Fig. 5.1. Consequently, an equivalent circuit with the same topology is used in the model develop here. The entire structure is modeled as a cascaded connection of the corresponding transmission lines, with the lumped T-junction

equivalent circuits in between. A unit cell equivalent circuit, repeated periodically to model the structure from Fig. 5.1, is illustrated in Fig. 5.5.

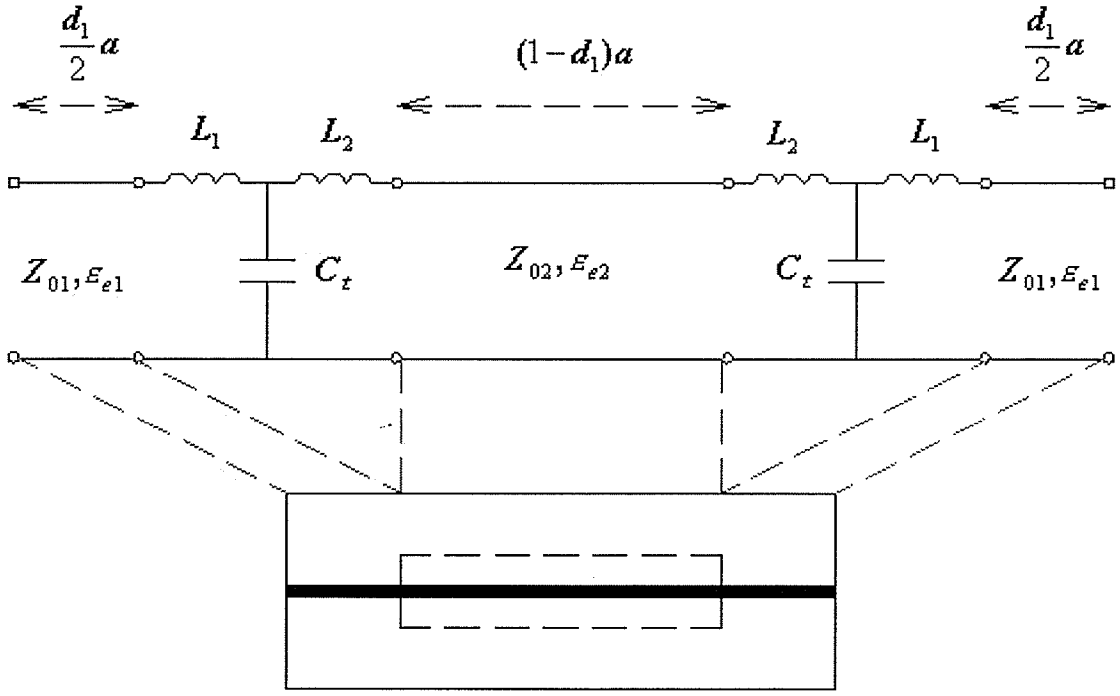

Fig. 5.5 Unit cell equivalent circuit for a microstrip line with periodically etched rectangles in the ground plane

The lumped equivalent circuits at the transitions are symmetrical around the central transmission line, which has a gap in the ground plane. Therefore, the positions of the lumped inductances at the two transition interfaces are reversed.

One way to determine the lumped element values in the model shown in Fig. 5.4 is to compare the transmission parameters of this model with the ones of the actual structure. The lumped elements values can be changed, until a satisfactory agreement with the full wave simulated parameters (as from "Ensemble") of the actual structure is obtained. A Matlab program is written for the purpose of estimating the lumped elements values for a

specified structure. Furthermore, the characteristic impedance and effective permittivity values of the perforated line sections are allowed to slightly change around their values estimated in section 5.1 (Z_c=104.08 Ω and ε_e=3.77), due to limited accuracy of the method used. The microstrip structures under study are similar to the structures from the previous chapter, except that they have 7 etched rectangles in the ground plane, instead of 5 circles. The rectangle period is $a = 14mm$ as before, while the structure length is increased from 86 *mm* to 114 *mm*, due to the larger number of perforations. The rectangle widths are kept constant at $w_r = 5mm$, which is about 9 times wider than the trace conductor on top of the substrate. The rectangle lengths are varied for different structures, in order to obtain desired bandwidth. The Matlab program is applied to the first structure under study, with rectangle lengths $l_r = 5mm$ each, therefore having 7 etched squares in the ground plane. The parameters obtained for this structure from the Matlab program, as well as given parameters, are labeled corresponding to Fig. 5.5, and their values are:

$C_t = 1.86 \times 10^{-13} F/m$ (5.4_a) $L_1 = 0$ (5.4_b)

$L_2 = 4.70 \times 10^{-10} H/m$ (5.4_c) $Z_{02} = 106.1\Omega$ (5.4_d)

$\varepsilon_{e2} = 2.95$ (5.4_e) $Z_{01} = 50\Omega$ (5.4_f)

$\varepsilon_{e1} = 7.21$ (5.4_g) $a = 14mm$ (5.4_h)

$d_1 = 9/14$ (5.4_i) $(1-d_1)a = l_r = 5mm$ (5.4_j)

where Z_{02} and ε_{e2} are optimized values, overriding the ones obtained in section 5.1.

The scattering parameters of the equivalent model structure are compared with the parameters obtained by the full wave simulation, as shown in Fig. 5.6.

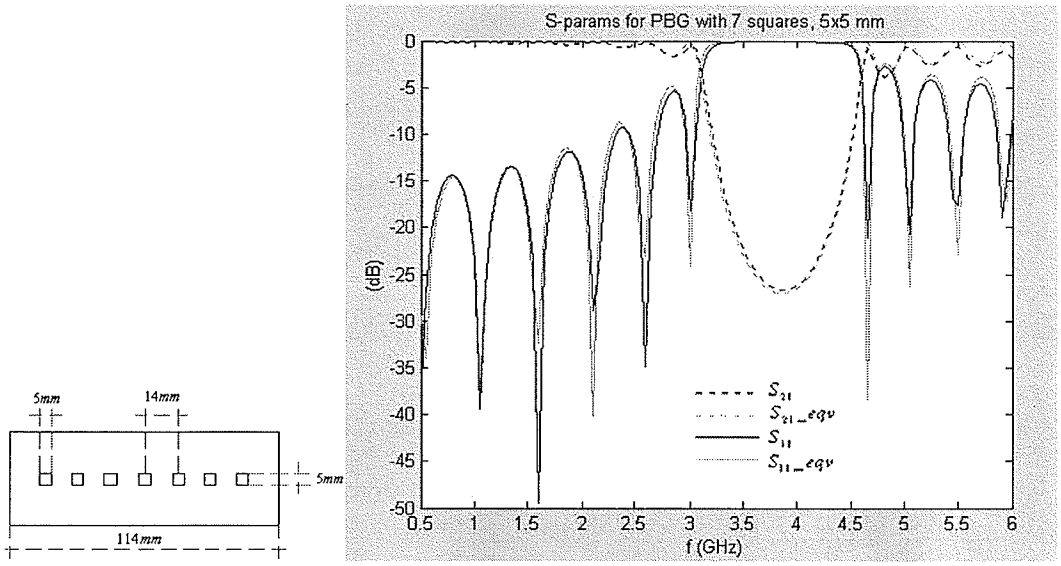

Fig. 5.6 Equivalent circuit and "Ensemble" simulated S-parameters for a 114 mm microstrip line with 7 etched 5x5 mm squares in the ground plane, spaced at 14 mm

The equivalent circuit scattering parameters are in excellent agreement with the simulated results. This shows the validity of the equivalent circuit approach, even when neglecting higher order mode analysis over the frequency range of interest. As expected, the rectangular ground plane perforations cause a frequency stopband, similar to the one of a circular PBG structure in the previous chapter. The filter $-3dB$ bandwidth for the rectangular PBG structure happens to be between $f_{lo} = 3.10GHz$ and $f_{hi} = 4.60GHz$, with the corresponding mean stopband frequency $f_c = 3.85GHz$. The entire stopband for this structure is slightly shifted down in frequency, as compared to the structure with 5 *mm* circular perforations. The reasons for this shift in frequency can be explained by

studying the phase characteristics of the equivalent circuit and the simulated rectangular structure, shown in Fig. 5.7.

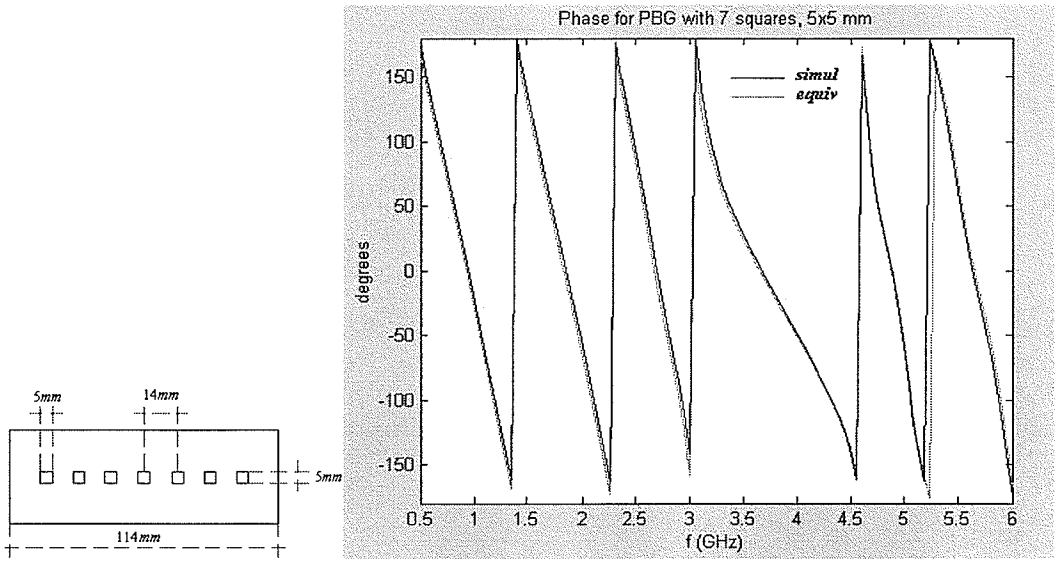

Fig. 5.7 Equivalent circuit and "Ensemble" simulated phase for a 114 mm microstrip line with 7 etched 5x5 mm squares in the ground plane, spaced at 14 mm

The phase characteristics are in excellent agreement also, confirming the validity of the equivalent circuit model. The effective permittivity for this PBG structure is estimated at specific frequencies from Fig. 5.6, and shown in table 5.1.

Table 5.1. Perforated transmission line effective permittivity values obtained from simulated S_{21} phase, for the structure with 7 etched squares having d=5mm and a=14mm

f_c (GHz)	f_1 (GHz)	f_2 (GHz)	Δf (GHz)	$\Delta\theta$ (°)	ε_e
1.83	1.40	2.25	0.85	343.17	8.710
2.65	2.30	3.00	0.70	317.54	10.99
3.80	3.05	4.55	1.50	339.70	2.741
5.63	5.25	6.00	0.75	354.14	11.91

The passband effective permittivity of this structure is even higher than the one of the corresponding circular PBG structure, while the stopband permittivity is lower. This observation is caused by more abrupt metallic discontinuities in the rectangular PBG structure, which affect the signal phase. In order to examine the effect of lumped elements in the equivalent circuit model from Fig. 5.5, the band plots for this model are generated and compared with the same model without the lumped elements, as shown in Fig. 5.8.

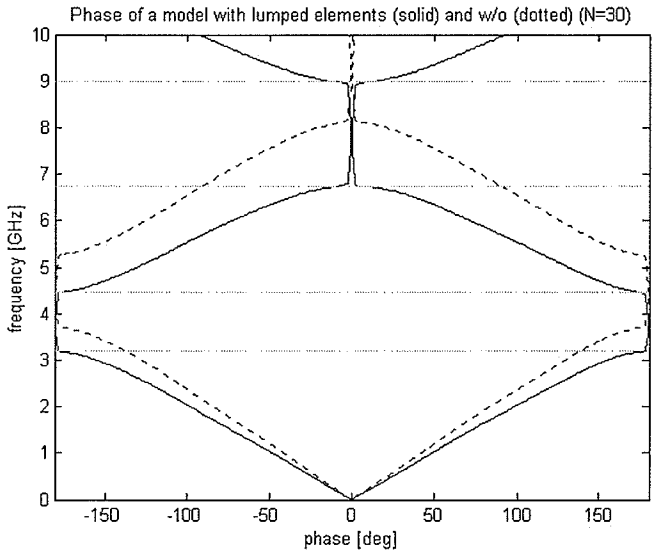

Fig. 5.8 Band plots for cascaded-lumped model (solid) of a microstrip line with etched 5x5 mm squares in the ground plane spaced at 14 mm, and the same model w/o lumped elements (dotted)

In order to generate a smooth plot with sharply defined bandgaps, the total of N=30 unit cell elements are used, and the phase change within a unit cell is shown in Fig. 5.8. Furthermore, the effective permittivity permittivities for both models were estimated by numerical differentiation of the phase plots in Fig. 5.8, and shown in Fig. 5.9. The effective permittivity low frequency approximation for the model without lumped

elements is estimated at $\varepsilon_{low\_f} = 5.47$, as given by (3.12), and shown as a dashed horizontal line in Fig. 5.9.

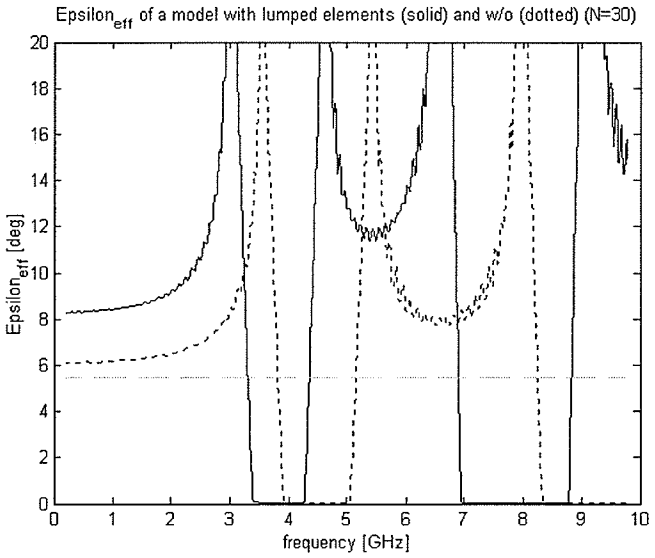

Fig. 5.9 Effective permittivities for cascaded-lumped model (solid) of a microstrip line with etched 5x5 mm squares in the ground plane spaced at 14 mm, and the same model w/o lumped elements (dotted)

Clearly from Fig. 5.8 and Fig. 5.9, the metallic discontinuities in the ground plane modeled as lumped elements, caused the increase in the phase change and therefore the effective permittivity as well, which resulted in the bandgap shift to lower frequency.

In order to validate the equivalent circuit model completely, the model parameters given by (5.4) have to be independent of the rectangle lengths, as well as the number of rectangles in the ground plane. For the purpose of validating the parameter independence of the rectangle lengths, the Matlab program is applied to the structure with 7 rectangles with lengths $l_r = 10mm$ each (rather than $5mm$), while keeping other dimensions the same. The scattering parameters of the equivalent model for this structure are compared with the parameters obtained by the full wave simulation, as shown in Fig. 5.10.

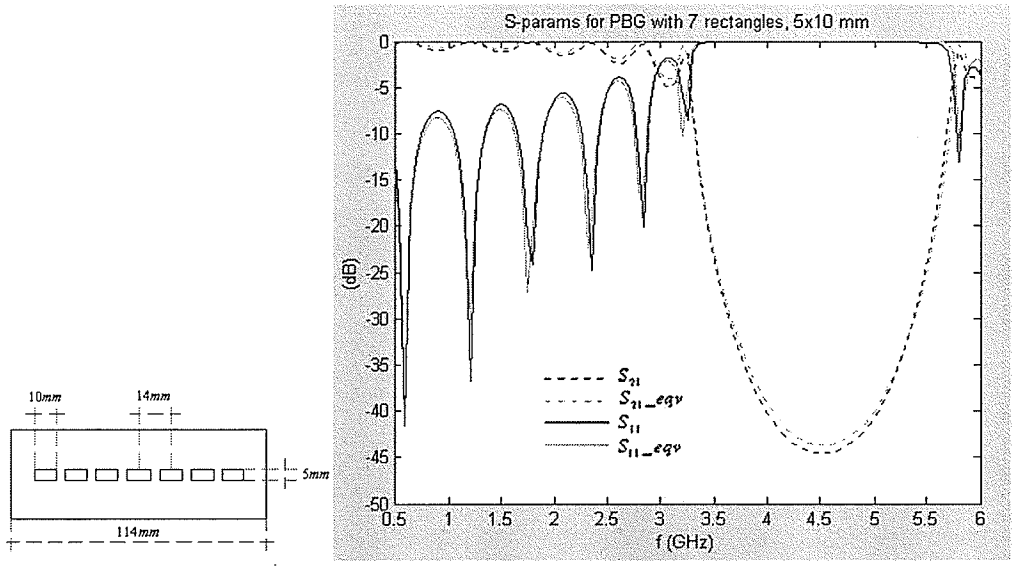

Fig. 5.10 Equivalent circuit and "Ensemble" simulated S-parameters for a 114 mm microstrip line with 7 etched 5x10 mm rectangles in the ground plane, spaced at 14 mm

The $-3dB$ stopband bandwidth of this structure falls between $f_{lo} = 3.25GHz$ and $f_{hi} = 5.75GHz$, while the mean stopband frequency is $f_c = 4.50GHz$. The corresponding phase characteristics for the same structure are shown in Fig. 5.11.

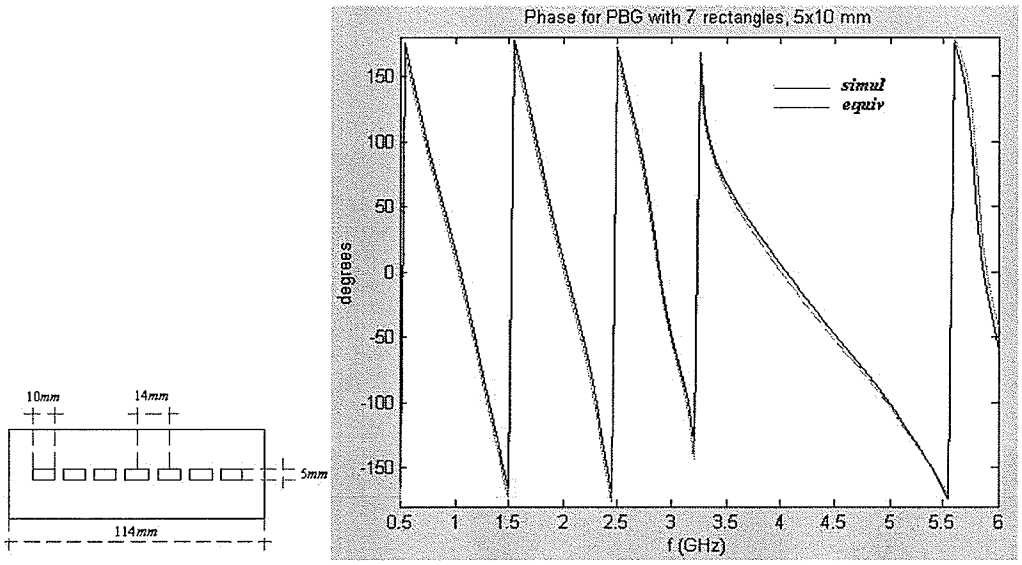

Fig. 5.11 Equivalent circuit and "Ensemble" simulated phase for a 114 mm microstrip line with 7 etched 5x10 mm rectangles in the ground plane, spaced at 14 mm

The equivalent circuit characteristics remain to be in a good agreement with the full wave simulated ones, confirming the model parameters independence of the rectangle lengths. The parameters proved to be independent of the number of perforations as well, yielding a good agreement for several structures with different number of ground plane rectangles.

Finally, we can apply the circuit theory to the equivalent circuit model, in order to obtain the voltage as a function of position along the line, for a given frequency. Another Matlab program was written, where the ABCD matrix of the whole structure was used to obtain the input voltage v_1 and current i_1, as per equation (2.11_b). The output normalized voltage and current are assumed to be $v_{out} = 1$ and $i_{out} = -1$, respectively, corresponding to a matched load impedance with its normalized value of $z_L = v_{out} / (-i_{out}) = 1$. Furthermore, the matrices ABCD_(z) were calculated for the partial structures extending from the input port to the points at chosen distances z along the structure. Having determined v_1, i_1 and ABCD_(z), the voltage and current along the line are obtained by rearranging (2.11_b). The Matlab program was run for the structure with 7 etched squares in the ground plane, whose scattering parameters plots are shown in Fig. 5.6 and Fig. 5.7. The magnitude and phase of the voltage along the structure $v(z)$ are obtained at a passband frequency of $f_1 = 1.68GHz$, and their values relative to the input voltage v_1 are shown in Fig. 5.12. Similarly, the relative $v(z)$ magnitude and phase plots obtained for a stopband frequency of $f_2 = 4GHz$ are shown in Fig. 5.13. The voltage magnitude and phase values at the output end match exactly the values from Fig. 5.6 and Fig. 5.7, respectively, at frequencies $f_1 = 1.68GHz$ and $f_2 = 4GHz$.

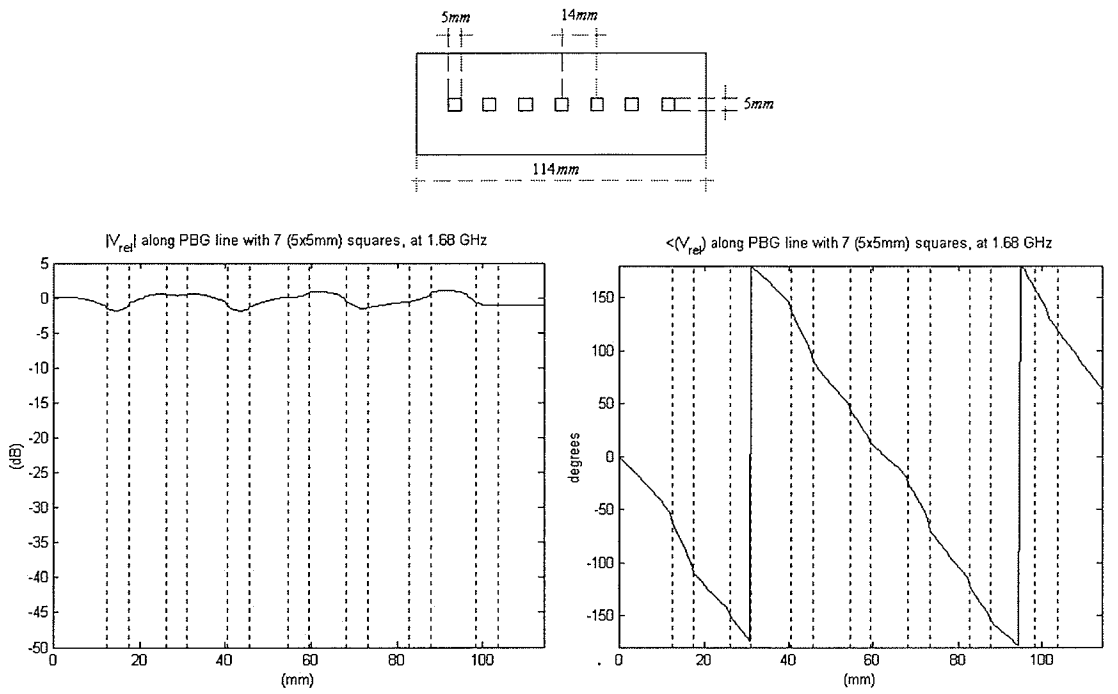

Fig. 5.12 Relative voltage magnitude (left) and phase (right) at f=1.68GHz, along a 114mm long microstrip line with 7 ground plane etched 5x5mm squares, spaced at a=14mm

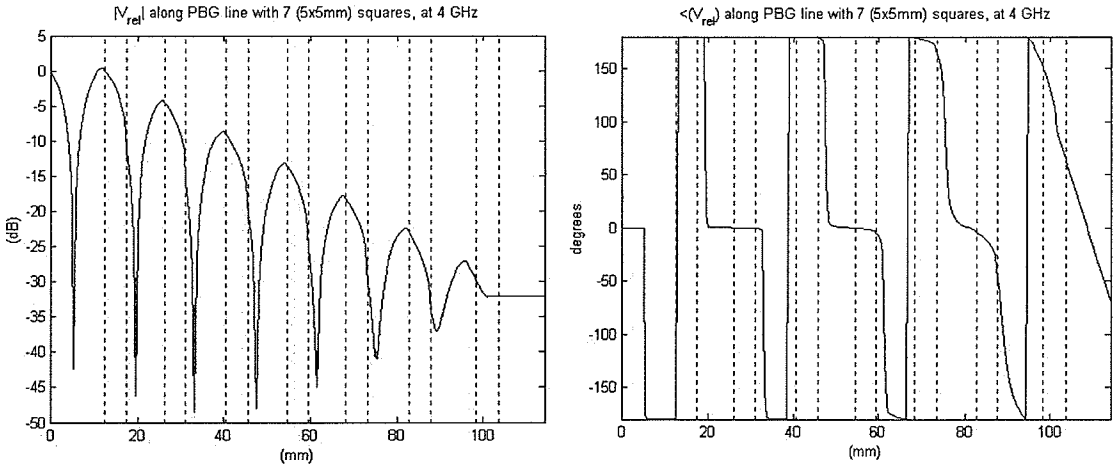

Fig. 5.13 Relative voltage magnitude (left) and phase (right) at f=4GHz, along a 114mm long microstrip line with 7 ground plane etched 5x5mm squares, spaced at a=14mm

The plots shown in Fig. 5.12 and Fig. 5.13 have a similar pattern, as the plots from Fig. 4.13-4.16, obtained by near-field scanning of the structure with *d*=5*mm* etched circles.

The voltage within the structure at a stopband frequency of 4*GHz* undergoes a linear decay on a logarithmic scale, as shown in Fig. 5.13 (left). Therefore, the voltage decays exponentially within the structure, representing an evanescent mode. Consequently, the phase characteristic of this mode is highly non-linear, as shown in Fig. 5.13 (right).

The equivalent circuit model proposed in this chapter exhibited an excellent agreement with the full wave simulated results, for frequencies below 6*GHz*. In order to establish the limiting frequency when the model is no longer valid for a particular example, the equivalent circuit results are compared with the "Ensemble" results for frequencies up to 14*GHz*. The structure studied is the one with 7 etched squares in the ground plane, as shown in Fig. 5.6. In order to improve readability, the plot in Fig. 5.14 shows only the transmission coefficients of the simulated and equivalent circuit results.

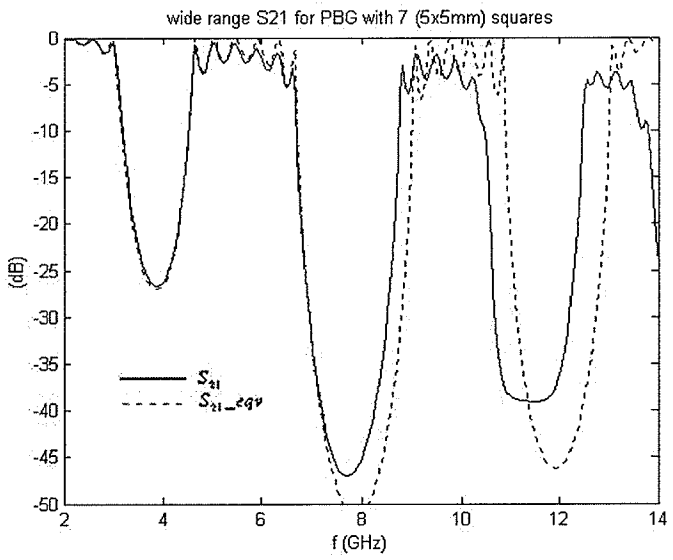

Fig. 5.14 Equivalent circuit and "Ensemble" simulated S21 for a 114 mm microstrip line with 7 etched 5x5 mm squares in the ground plane, spaced at 14 mm, 2<f<14GHz

Clearly from Fig. 5.14, the "Ensemble" simulated transmission coefficient (solid line) starts to decay even within the passband regions, for frequencies above $9GHz$ approximately. On the other hand, the equivalent circuit transmission coefficient has an increased ripple for frequencies above approximately 9 GHz, but the overall pattern does not seem to decay. Therefore, for this particular structure, we conclude that model is valid for frequencies up to 9 GHz, approximately. In order to match the simulated results outside of this frequency range, the equivalent circuit parameters would need to be modified.

5.3 Conclusion

In this chapter microstrip transmission lines with rectangular ground plane perforations were studied. It was shown that over a certain frequency range, these 2-D structures can be effectively modeled by 1-D equivalent circuits, consisting of cascaded sections of transmission lines, and lumped reactive elements at the transitions between the line sections. The characteristic impedance and the effective permittivity of line sections with the etched rectangles in the ground plane were estimated by solving the electrostatic Laplace boundary problem. The remaining line sections are considered to be regular unperturbed microstrip lines. Finally, a Matlab program was developed to estimate the lumped reactive element values, needed for the equivalent circuit model.

The equivalent circuit transmission parameters were in excellent agreement with the full wave simulated results within a specified frequency range, regardless of the number of rectangular perforations or their lengths. The circuit parameters were not frequency

dependent over the range used in the examples, proving that a single mode (quasi-TEM) of operation can be assumed for the studied structures. Once the equivalent circuit parameters are determined, the structure transmission parameters were obtained much faster than it was the case with the "Ensemble" full wave simulator. However, in order to make this method practical, the empirical expressions need to be developed for easy determination of the equivalent circuit parameters. One way of finding these expressions would be to estimate the parameters for different geometries, using the methods presented in this chapter. In the next step, the expressions for the parameters in terms of dimensions would be determined numerically, where the parameter values obtained would be within the specified error, for all considered geometries.

Chapter 6

Conclusion

6.1 Summary

This thesis provided a comprehensive study of PBG structures used in microstrip transmission line stopband filters. The PBG structures used in the designs and simulations in this thesis can be summarized into two groups, namely the Dielectric Contrasting PBG structures and the Microstrip Ground Plane PBG structures. The latter group consists of two different subgroups, the circular and rectangular ground plane perforated structures.

The Dielectric Contrasting PBG structures studied in detail were microstrip lines with periodic multilayer substrates. The first method for analysis of these structures was based on "Photonic Crystal" theory for an infinitely long dielectric multilayer structure. A numerical method for fast localization of the frequency bandgap was developed. The second method was based on the network theory, modeling these structures by a cascaded connection of transmission lines with different parameters. The results from both methods were conclusive, as demonstrated on a specific example.

Microstrip transmission lines with circular ground plane perforations were studied next. It was shown that the bandgap properties are dependent on the period and diameter of the etched ground plane circles. The effective permittivities of these structures were found to be higher in the passband, and lower in the stopband frequency region, than the effective

permittivities of corresponding unperturbed microstrip lines. In order to confirm the simulation results, several microstrip structures with different number of circular perforations and diameters, were fabricated and tested. The measured data showed a good agreement with the full wave simulated results. Furthermore, the near-field probe scanning plots were created for the fabricated structures, giving more insight into the field configurations on these structures.

Finally, microstrip transmission lines with rectangular ground plane perforations were studied as well. Since the simulated results for the structures with circular perforations exhibited a good agreement with the measured data, the structures with rectangular perforations were analyzed by simulation only. These structures exhibited similar properties as the structures with circular ground plane perforations. However, due to the uniform cross section of the line segments with etched rectangles in the ground plane, a 1-D equivalent circuit was developed for these 2-D structures. The circuit consisted of cascaded connection of transmission line segments, with a reactive lumped elements transition in between. The values of the equivalent circuit parameters are estimated, and an excellent agreement between the equivalent circuit transmission characteristics and ones obtained by the full wave simulator is achieved, over the specified frequency range. The equivalent circuit model developed needed considerably less time to generate the transmission parameters, compared with the "Ensemble" full wave simulator. The equivalent circuit parameters proved to be independent of the number of rectangular perforations or their lengths, confirming the model validity.

6.2 Future Research

Some suggestions for future work in the area of PBG microstrip line structures are given below.

- Empirical formulas development for estimating the equivalent circuit parameters of microstrip lines with rectangular ground plane perforations.
- Development of tunable PBG microstrip line filters.
- Use of two-dimensional PBG structures to suppress the surface waves within the passband frequency range of a filter.

References

[1] F. Gardiol, "Microstrip Circuits", John Wiley & Sons, Inc. 1994.

[2] J. D. Joannopoulos, R. D. Meade, J. N. Winn, "Photonic Crystals – Molding the Flow of Light", Princeton University Press, 1995.

[3] M. N. O. Sadiku, "Elements of Electromagnetics", Oxford University Press, 1995.

[4] Lecture notes from 24.429, "Microwave Engineering"

[5] D. M. Pozar, "Microwave Engineering", John Wiley and Sons, Inc. 2nd edition, 1998.

[6] V. Radisic, Y. Qian, R. Coccioli and T. Itoh, "Novel 2-D Photonic Bandgap Structure fir Microstrip Lines", IEEE Microwave and Guided Wave Letters, Vol. 8, No. 2, Feb. 1998. pp. 69-71

[7] T. Lopetegi, M. A. G. Laso, M. J. Erro, M. Sorolla and M. Thumm, "Analysis and Design of Periodic Structures for Microstrip Lines by Using the Coupled Mode Theory", IEEE Microwave and Wireless Components Letters, Vol. 12, No. 11, Nov. 2002, pp. 441-442

[8] S. G. Johnson, J. D. Joannopoulos, "Photonic Crystals – The Road from Theory to Practice", Kluwer Academic Publishers, 2002.

[9] F. R. Yang, K. P. Ma, Y. Qian and T. Itoh, "A Uniplanar Compact Photonic-Bandgap (UC-PBG) Structure and Its Applications for Microwave Circuits",

Transactions on Microwave Theory and Technique, Vol. 47, No. 8, Aug. 1999, pp. 1509-1514

[10] Y. Qian and T. Itoh, "Planar Periodic Structures for Microwave and Millimeter Wave Circuit Applications", Microwave Symposium Digest, 1999 IEEE MTT-S International, Vol. 4, 1999, pp. 1533-1536

[11] T. Kim and C. Seo, "A Novel Photonic Bandgap Structure for Low-Pass Filter of Wide Stopband", IEEE Microwave and Guided Wave Letters, Vol. 10, No. 1, Jan 2000, pp. 13-15

[12] R. D. Meade, A. M. Rappe and J. D. Joannopoulos, "Nature of Photonic Bandgap: Some Insight from a Field Analysis", J. Opt. Soc. Am. B/Vol. 10, No. 2, February 1993, pp. 328-332

[13] T. Y. Yun and K. Chang, "Uniplanar One-Dimensional Photonic-Bandgap Structures and Resonators", IEEE Transactions on Microwave Theory and Technique, Vol. 49, No. 3, March 2001, pp. 549-553

[14] H. Y. D. Yang, "Theory of Microstrip Lines on Artificial Periodic Substrates", IEEE Transactions on Microwave Theory and Technique, Vol. 47, No. 5, May 1999, pp. 629-635

[15] A. Serpenguzel, "Transmission Characteristics of Metallodielectric Photonic Crystals and Resonators", IEEE Microwave Wireless Components Letters, Vol. 12, No. 4, April 2002, pp. 134-136

[16] Y. Fu, G. Zhang and N. Yuan, "A Novel PBG Coplanar Waveguide", IEE Microwave and Wireless Components Letters, Vol. 11, No. 11, Nov. 2001, pp. 447-449

[17] J. Yoon and C. Seo, "Improvement of Broadband Feedforward Amplifier Using Photonic Bandgap", IEEE Microwave and Wireless Components Letters, Vol. 11, No. 11, Nov. 2001, pp. 450-452

[18] S. T. Chew and T. Itoh, "PBG-Excited Split-Mode Resonator Bandpass Filter", IEEE Microwave and Wireless Components Letters, Vol. 11, No. 9, Sep. 2001, pp. 364-366

[19] C. Chang and W. Hsu, "Photonic Bandgap Dielectric Waveguide Filter", IEEE Microwave and Wireless Components Letters, Vol. 12, No. 4, April 2002, pp. 137-139

[20] S. Mao and M. Chen, "Propagation Characteristics of Finite-Width Conductor-Backed Coplanar Waveguides with Periodic Electromagnetic Bandgap Cells", IEEE Transactions on Microwave Theory and Techniques, Vol. 50, No. 11, Nov. 2002, pp. 2624-2628